Determination of the hydrogen fugacity during electrolytic charging of steel

Qian Liu[1,2], Aleks D. Atrens[3], Zhiming Shi[2,4], Kim Verbeken[5], Andrej Atrens[1,2,*]

[1] The University of Queensland, Materials Engineering, School of Mechanical and Mining Engineering, St Lucia, Qld 4072, Australia

[2] The University of Queensland, Queensland Centre for Advanced Materials Processing and Manufacturing (AMPAM), School of mechanical and Mining Engineering, Brisbane, Qld 4072, Australia

[3] The University of Queensland, The Queensland Geothermal Energy Centre of Excellence, School of Mechanical and Mining Engineering, St Lucia, Qld 4072, Australia

[4] The University of Queensland, Defence Materials Technology Centre, Brisbane, Qld 4072, Australia

[5] Ghent University, Department of Materials and Science Engineering, Technologiepark 903, B-9052 Zwijnaarde (Ghent), Belgium

* Corresponding author, Andrejs.Atrens@uq.edu.au, T: +61 7 3365 3748

Abstract

This work studied the determination of the hydrogen fugacity during electrolytic charging. With a virgin surface, there were irregular permeation transients, attributed to irreproducible surface conditions. Cathodic pre-charging conditioned the entry side to a stable state. Permeability transients were used to measure the critical parameters in the thermodynamic relationship between hydrogen activity and electrochemical potential. At the same overpotenial, the hydrogen fugacity in the pH 12.6 0.1 M NaOH solution was higher than that in the pH 2 0.1M Na_2SO_4 solution, attributed to differences in (i) the hydrogen evolution reaction, (ii) the surface state, and (iii) the true surface area.

Keywords: A. Steel, B. hydrogen permeation, B. potentiostatic

1. Introduction

1.1 Importance

Hydrogen has caused catastrophic failures in service, and there are many studies into the influence of hydrogen on the mechanical properties of steels [1-64]. Many of these studies would be more relevant if the hydrogen charging conditions were better defined. It has even been demonstrated for different kinds of steels that under specific conditions, electrolytic

hydrogen charging can damage the sample during charging. These conditions depend on (i) the chemical composition of the steel, (ii) its microstructure, (iii) the electrolyte and (iv) the sample preparation [65, 66]. This damage minimizes the relevance of subsequent tests on the hydrogen influence of the mechanical properties of these steels.

Two methods have been used to simulate the hydrogen in steels which are used in hydrogen environments: (i) electrochemical charging typically at room temperature [35, 67-73] and (ii) gas phase hydrogen charging, typically at elevated temperatures [63, 74]. Electrochemical charging at room temperature causes different traps to become active compared with gaseous hydrogen charging at elevated temperature [75]. Furthermore, the manner of hydrogen charging influences its subsequent desorption, and is an important factor to consider during thermal desorption spectroscopy measurements [76, 77].

In many studies, however, no attempt has been made to estimate the hydrogen activity.

Nevertheless, there is a conceptually simple approach by which to determine the hydrogen activity for any particular hydrogen charging condition, by the combined use of thermodynamics [78-81] and the use of permeability experiments [78, 82-92]. The aim of the present research was to evaluate this approach to define the hydrogen charging condition during the electrolytic charging of steels.

1.2 Conceptual approach

By definition, electrolytic charging conditions are equivalent to gaseous charging at room temperature if both charging methods produce the same activity of hydrogen dissolved in the steel inside the surface of the steel during charging. The establishment of equivalence between gaseous charging and electrolytic hydrogen charging at a constant potential and at the same temperature, was considered by Atrens et al. [78] based on [79-81], and the treatment herein follows that described therein. What is needed is a methodology by which to determine the hydrogen activity (or pressure) during gaseous hydrogen charging that is equivalent to the hydrogen activity during the electrolytic charging. This work considers that the gaseous hydrogen charging is the same as the electrolytic charging at the same temperature.

The Nernst equation provides the fundamental thermodynamic relationship between the electrochemical potential and the activities of reactants and products of any reaction [80, 93,

94], including the hydrogen evolution reaction, which can be written as follows in an acid solution (Eq. (1)), or an alkaline solution (Eq. (2)):

$$2H^+ + 2e^- \rightarrow H_2 \quad (1)$$

$$2H_2O + 2e^- \rightarrow H_2 + 2OH^- \quad (2)$$

Thus, the Nernst equation can be used to provide the relationship between the hydrogen activity (or pressure, or fugacity) at the electrode surface and the applied potential, E_c, as suggested by Bockris and Subramanyan [81], and as is also clear from standard texts such as Jones [93], Pourbaix [95], Bockris and Reddy [80], Marcus [96], and Kaesche [94]. The relevant expression between the hydrogen fugacity, f_{H_2}, under hydrogen cathodic charging conditions, and the constant applied potential, E_c [78, 81] can be written as follows:

$$f_{H_2} = A \exp\left(\frac{-\eta F}{\zeta RT}\right), \quad (3)$$

where η is the overpotential of the hydrogen evolution reaction, F is the Faraday, R the gas constant, T the absolute temperature, and A and ζ are constants, related to the mechanism of the hydrogen evolution reaction (HER), which is discussed later. There is also a list of symbols at the end of this paper. The overpotential, η, is given by

$$\eta = E_c - E_H^0 \quad (4)$$

where E_H^0 is the equilibrium potential at the steel surface in the charging solution of the hydrogen evolution reaction at a fugacity of one atmosphere pressure, and E_c is the applied potential. E_H^0 can be determined experimentally [78], or can be also calculated using the Nernst equation [97] as follows:

$$E_H^0 = -0.0591 \times pH - 0.0295 \log f_{H_2}, \quad (5)$$

where pH is the negative logarithm of the hydrogen ion concentration of the charging solution (i.e. a measure of the solution acidity), and $f_{H_2} = 1$ atm, so that the second term in Eq. (5) is equal to zero. Note that the fugacity is the same as the pressure at low pressures.

Eq. (3) provides an expression that links the electrochemical potential to the hydrogen activity at the electrode surface. It is expected that the hydrogen liberated by the hydrogen evolution reaction at the electrode surface acts in the same manner, as does gaseous hydrogen,

once the hydrogen has entered the steel. There is no reason to expect that there is any memory in the hydrogen that causes a difference in behaviour according to the hydrogen source. Indeed, it is expected that hydrogen liberated by an electrochemical reaction acts in exactly the same manner as does originally gaseous hydrogen.

The hydrogen concentration dissolved in the steel in equilibrium inside the steel surface, C_H, can be evaluated using Sievert's law:

$$C_H = S\sqrt{f_{H_2}} \tag{6}$$

where S is the solubility constant, and the hydrogen activity needs to be expressed using hydrogen fugacity, f_{H_2}, rather than hydrogen pressure P_{H_2} [81, 98], whenever the hydrogen activity or pressure is large. Literature data [99] indicate that $S = 3.8\times10^{-3}$ mol m^{-3} atm$^{-1/2}$ at 25 °C, for pure iron for conditions of gaseous hydrogen charging, when the fugacity, f_{H_2}, is expressed in units of atm, as is done throughout this paper, and as also done by Pourbaix [95] for the units of hydrogen pressure. For small hydrogen pressures, the hydrogen fugacity is equal to the hydrogen pressure. It is stressed that Eq. (6) applies to equilibrium conditions.

The definition for fugacity used herein is that the fugacity is the pressure of an ideal gas that has the same chemical potential as the real gas [100], and so fugacity has the same units as pressure. Bockris and Subramanyan [81] have provided a relationship between fugacity and pressure for hydrogen.

In an ideal electrochemical permeability experiment [82], the hydrogen concentration on the entry side is proportional to the current density at steady state at the exit side i_∞, and is given [101] by

$$C_H = \frac{i_\infty L}{FD} \tag{7}$$

where i_∞ is the steady-state permeation current density at the exit side for a given negative potential at the entry side; L is the specimen thickness; F is Faraday constant; and D is the hydrogen diffusion coefficient in the steel on which the permeability experiment was carried out. Eq. (7) requires that there is no impediment for hydrogen entry into the steel specimen, that there is no trapping of hydrogen inside the steel specimen, that there is no impediment for hydrogen egress from the specimen, and that i_∞ (the steady-state current density at the exit side) is a good measure of all the hydrogen egressing the steel specimen on the exit side.

Under conditions that (i) Sievert's law applies in both gas phase permeation studies and electrolytic charging studies, (ii) equilibrium conditions are attained on the charging side, and (iii) an ideal permeation transient is measured, then

$$i_\infty = \frac{FDS}{L}\left(f_{H_2}^e\right)^{1/2} = \frac{FDS}{L}\left(A\exp\left(-\frac{\eta F}{\zeta RT}\right)\right)^{1/2} \tag{8}$$

where $f_{H_2}^e$ is the fugacity during electrolytic charging. Eq. (8) provides a simple test of the applicability of the approach. Eq. (8) indicates that the plot of $\ln i_\infty$ and η should be linear, which was verified by the results in the study of Atrens et al. [78] for pure Ni.

In such a case, the parameters A and ζ can be evaluated from the relationship between η and i_∞, in particular ζ can be evaluated as [78]:

$$\zeta = -\frac{1}{2}\frac{F}{RT}\frac{\partial\eta}{\partial\ln i_\infty}, \tag{9}$$

and the hydrogen fugacity during electrochemical charging is defined by Eq. (3), using the experimentally determined values of A and ζ.

1.3 Important details

The determination of the hydrogen fugacity during electrolytic charging of steels can be made difficult by experimental problems that influence the values measured for C_H and D. Surface impedance to hydrogen charging by the state of the surface (including the state of surface oxides and hydroxides) can influence the attained surface hydrogen concentration, C_H. Trapping of hydrogen in the steel, and the quality of Pd coating on the exit side of the permeability specimen, can both influence the measured apparent hydrogen diffusion coefficient, D. Nevertheless, there are indications from the literature that both these difficulties can be overcome for steels.

Zakroczymski et al. [102-104] indicated that surface effects may be eliminated or at least stabilized for steel by a sufficiently-long uninterrupted cathodic polarisation. The detailed examination of the surface changes, and changes to surface oxides/hydroxides, are beyond the scope of the present research. Those interested might consider the following references as a starting point [104-112].

Trapping effects can be minimised by successive transients with partial increasing or decreasing cathodic polarisation [78], and by the use of an annealed pure Fe specimen (or equivalently a low interstitial steel), which has a minimum of hydrogen traps.

It has been found [79-81, 113-116] that the hydrogen evolution reaction, (Eq. (1) or Eq. (2)) at a metal surface, has the following three steps in an alkaline solution:

$$H_2O + M + e^- \rightarrow MH_{ads} + OH^- \quad (10)$$

$$2MH_{ads} \rightarrow H_2 + 2M \quad (11)$$

$$MH_{ads} + H_2O + e^- \rightarrow H_2 + OH^- + M \quad (12)$$

Eq. (10) is the electrochemical discharge of hydrogen from a water molecule at the metal surface (M), to produce a hydrogen atom adsorbed on the metal surface, MH_{ads}. Eq. (10) typically occurs for low overpotentials, when there is a relatively low coverage of the surface by hydrogen. Such an adsorbed H atom can move around on the metal surface, until two adsorbed hydrogen atoms combine by Eq. (11), to produce a molecule of hydrogen, which can leave the surface as a gas in combination with other hydrogen molecules. As the hydrogen surface coverage becomes appreciable, electrochemical desorption by Eq. (12) becomes increasingly probable, and hydrogen adsorbed atoms can leave the metal surface by two reactions, namely by Eq. (11) and Eq. (12). Note that the sum of Eq.(10) and Eq. (11) results in the same reaction as Eq. (2). Similarly, the sum of Eq. (10) and Eq. (12) also results in the same reaction as Eq. (2)

The hydrogen atoms adsorbed on the metal surface can also enter the metal and be dissolved in the metal, MH_{abs}, by the following equilibrium:

$$MH_{ads} \Leftrightarrow MH_{abs} \quad (13)$$

Bockris and Subramanyan [81] considered the possible combinations of the steps represented by Eqs. (10) to (12), and derived idealised equilibrium expressions relating the hydrogen fugacity and the overpotential. For the case of coupled electrochemical discharge-chemical recombination (i.e. coupled Eqs. (10) and (11)), they deduced the following expression for the hydrogen fugacity:

$$f_{H_2} = 10^{-1.5} \exp\left(\frac{-\eta F}{2RT}\right) = 0.0316 \exp\left(\frac{-\eta F}{2RT}\right) \quad (14)$$

Note that Eq. (14) has been corrected for the algebraic error in [81]. This derivation assumed that the potential barrier to the hydrogen evolution reaction was symmetrical. For the case of coupled electrochemical discharge-electrochemical desorption (i.e. coupled Eqs. (10) and (12)), their analysis indicated that the hydrogen fugacity becomes a constant independent of the overpotential when these conditions become established. The implication is that the hydrogen fugacity increases with overpotential until these conditions became established.

Bockris et al. [79] considered hydrogen evolution kinetics and hydrogen entry into pure Armco iron from *inter alia* 0.1 M NaOH. They concluded that their data, including their permeability transients, were consistent with hydrogen evolution by a coupled discharge-recombination mechanism at low overpotentials ($|\eta| < 0.275$ V), (i.e. coupled Eq. (10) and Eq. (11)), and that fast electrochemical discharge (i.e. Eq. (12)) becomes important at higher overpotentials ($|\eta| > 0.275$ V), despite the fact that Bockris and Subramanyan [81] deduced that the fugacity becomes constant independent of the overpotential for the case of coupled electrochemical discharge-electrochemical desorption (i.e. coupled Eqs. (10) and (12)). Their data, following the above analysis, leads to the following evaluation of fugacity with overpotential, for pure Armco iron in 0.1 M NaOH (D = 7.5×10^{-5} cm^2 s^{-1} [99, 104], S (hydrogen solubility constant) = 3.8×10^{-3} mol m^{-3} $atm^{-1/2}$ at 25 °C, when the fugacity, f_{H_2}, is expressed in units of atm [99]):

$$f_{H_2} = 0.022 \exp\left(-\frac{\eta F}{2.0RT}\right), \text{ for } |\eta| < 0.275 \text{ V, and} \quad (15)$$

$$f_{H_2} = 1.262 \exp\left(-\frac{\eta F}{11.17RT}\right), \text{ for } |\eta| > 0.275 \text{ V.} \quad (16)$$

Note the good agreement of the experimental data, Eq.(15) to the theoretical expression (Eq.(14)) with the exception that the experimental data gave a value of the pre-exponential factor somewhat lower than that expected from the theoretical expression [81]. See however the comment after Eq. (23) below.

The relationship between fugacity and overpotential is expressed as two equations (Eqs. (15) and (16)) with a sharp knee purely for convenience. In reality there is expected to be a smooth transition between the two equations. This observation applies throughout this research.

1.4 Summary of approach

The approach is summarised in Fig. 1 (adapted from [96]). Permeation experiments allow measurement of the hydrogen concentration, C_H, dissolved in the steel on the entry side of a permeability specimen by means of Eq. (7). The hydrogen concentration, C_H, depends critically on the details of the hydrogen evolution reaction on the steel surface, and cannot be measured by electrochemical measurements on the entry side of the permeability specimen. Furthermore, the permeability experiments allow determination of how C_H varies with the overpotential on the entry side of the permeability specimen, and such experiments allow the determination of the parameters A and ζ in Eq. (3).

Note that, as indicated above, the state of the surface, and in particular surface oxides/hydroxides, probably plays an important role.

Further important insights about the hydrogen evolution reaction can be obtained from the experimentally measured relationship between the steady state permeation current density, i_∞, and the current density of hydrogen evolution on the specimen surface, i_c.

1.5 Aims

The aims of the present research were:

(i) to study how to determine the hydrogen fugacity in steels during electrolytic hydrogen charging at constant potential in two relatively-mild hydrogen-charging environments: (a) 0.1M NaOH solution, pH 12.6, and (b) acidified pH 2 0.1M Na_2SO_4 solution (as used in our prior research [42] to study hydrogen embrittlement of medium strength steels),

(ii) to consider a reaction sequence approach to determine the relationship between hydrogen fugacity, f_{H_2}, and overpotential η,

(iii) to consider the applicability of the fugacity so determined to the hydrogen fugacity during mechanical testing for hydrogen embrittlement,

(iv) to consider the applicability of the use of low interstitial steel (i.e. essentially pure iron) as a model material, with the expectation that the hydrogen evolution reaction on the pure iron surface is essentially the same as on the surface of another type of steel,

(v) to consider the influence of the surface state of the steel, and the importance of cathodic precharging [102-104], and

(vi) to consider the applicability to literature data of the methodology developed to determine hydrogen fugacity during electrochemical hydrogen charging.

2. Theory - reaction sequence approach

2.1 Equations

Bockris and Subramanyan [81] considered special cases for particular combinations of the reactions given by Eqs. (10), (11), (12) and (13). They made a significant contribution by pioneering the approach to the understanding of the hydrogen evolution reaction. An alternative approach is to consider the thermodynamic relationship between overpotential and H_{ads} when all three reactions given by Eqs. (10), (11) and (12) are possible. More details of this general approach can be gleaned from chemical engineering handbooks, such as that of Levenspiel [117].

For evolution of hydrogen on an iron surface, it is postulated that three major reactions define the reaction rate, provided in their *elementary* forms as follows:

$$H^+ + e^- + M \underset{k_a'}{\overset{k_a}{\rightleftharpoons}} MH_{ads} \quad \text{(A)}$$

$$2MH_{ads} \underset{k_b'}{\overset{k_b}{\rightleftharpoons}} 2M + H_2 \quad \text{(B)}$$

$$H^+ + e^- + MH_{ads} \underset{k_c'}{\overset{k_c}{\rightleftharpoons}} M + H_2 \quad \text{(C)}$$

where the k_x terms are the forward and backward reaction rate constants.

Bockris and Subramanyan [81] evaluated this system by defining surface coverage of adsorbed hydrogen on the metal surface (i.e. the proportion of surface sites occupied by MH_{ads} species as θ). This was assumed to be in equilibrium with absorbed H_2, the concentration of which can be characterised by an associated fugacity, defined via:

$$\left(\frac{\theta}{1-\theta}\right)^2 = \left(\frac{\theta_R}{1-\theta_R}\right)^2 f_{H_2} \quad (17)$$

where θ_R is the surface hydrogen coverage at 1 atm pressure.

The value of θ can be defined for any system at **steady state** by evaluating the forward and backward reactions of the system defined by reactions A, B, and C as per Eq. (17):

$$\frac{\delta\theta}{\delta t} = 0 = 2k_a C_{H^+}(1-\theta)\exp\left(-\alpha_a \frac{VF}{RT}\right) + k_b'(1-\theta)^2\sqrt{p_{H_2}} + 2k_c'(1-\theta)p_{H_2}\exp\Big((1-\alpha_c)\frac{VF}{RT}\Big) - 2k_a'\theta\exp\left((1-\alpha_a)\frac{VF}{RT}\right) - k_b\theta^2 - 2k_c C_{H^+}\theta\exp\left(-\alpha_c \frac{VF}{RT}\right) \quad (18)$$

Note that the rates for reactions A and C are multiplied by two to match the rates associated with reaction B. For all values of overpotential of interest in this work, the rates of the reverse reactions for A and C are negligible as the exponential term for the reverse reaction quickly becomes negligible. The reverse rate for reaction B can also be assumed negligible.

Consequently, the steady state condition can be defined by:

$$2k_a C_{H^+}(1-\theta)\exp\left(-\alpha_a \frac{VF}{RT}\right) = k_b\theta^2 + 2k_c C_{H^+}\theta\exp\left(-\alpha_c \frac{VF}{RT}\right) \quad (19)$$

This equation can be solved explicitly by rearranging into a quadratic equation. However the analytic solution of the resulting equations becomes exceedingly complex. Instead, it is practical to examine the limiting cases where the forward reaction rates of either reaction B or reaction C are dominant.

2.2 Low values of overpotential

For low values of overpotential, η, the forward rate of reaction B is much greater than the forward rate of reaction C, i.e:

$$k_b\theta^2 \gg 2k_C C_{H^+}\theta\exp\left(-\alpha_a \frac{VF}{RT}\right) \quad (20)$$

Eq. (19) can be simplified to:

$$2k_a C_{H^+}(1-\theta)\exp\left(-\alpha_a \frac{VF}{RT}\right) = k_b\theta^2 \quad (21)$$

which resolves to:

$$\frac{\theta^2}{1-\theta} = \frac{2k_a C_{H^+}\exp\left(-\alpha_a \frac{VF}{RT}\right)}{k_b} \quad (22)$$

which, for small values of θ, is:

$$\left(\frac{\theta}{1-\theta}\right)^2 = \frac{2k_a C_{H^+}\exp\left(-\alpha_a \frac{VF}{RT}\right)}{k_b} = \frac{2k_a C_{H^+}\exp\left(-\alpha_a \frac{V_{R,a}F}{RT}\right)}{k_b}\exp\left(-\alpha_a \frac{\eta F}{RT}\right) \quad (23)$$

Bockris and Subramanyan [81] evaluated this expression by assessing the conditions at the boundary between the linear relation between *i* and η, and the Tafel-slope relation (taken as $\eta = 2.303RT/F$). While this is reasonably likely to be linear, it is not entirely convincing that this should be the boundary of the Tafel slope. This is probably somewhat arbitrary, and the resulting constant depends on this choice (i.e. the $10^{-3\alpha_a}$ pre-expontential term in Eq. (14) which is equal to $10^{-1.5}$ if α_a is equal to 0.5). That is, a slightly different assumption would lead to a slightly different pre-exponential term in Eq. (14) and an assumption could be chosen so that the theoretical expression (i.e Eq. (14)) agreed better with that experimentally determined in Eq. (15).

Nevertheless, this assumption is accepted. In the linear region, reaction A is reversible, and consequently:

$$2k_a C_{H^+}(1-\theta_{lin})\exp\left(-\alpha_a \frac{VF}{RT}\right) = 2k'_a \theta_{lin}\exp\left((1-\alpha_a)\frac{VF}{RT}\right) \quad (24)$$

$$\left(\frac{\theta_{lin}}{1-\theta_{lin}}\right) = \frac{k_a C_{H^+}}{k'_a}\exp\left(-\frac{VF}{RT}\right) \quad (25)$$

Because the reversible surface coverage of MH_{ads} species is defined as:

$$\left(\frac{\theta_R}{1-\theta_R}\right) = \frac{k_a C_{H^+}}{k'_a}\exp\left(-\frac{V_{R,a}F}{RT}\right) \quad (26)$$

The linear region consequently relates surface coverage to overpotential by:

$$\left(\frac{\theta_{lin}}{1-\theta_{lin}}\right)^2 = \left(\frac{\theta_R}{1-\theta_R}\right)^2 \exp\left(-\frac{2\eta F}{RT}\right) \quad (27)$$

Combination of Eqs. (23) and (27), and substituting $\eta = 2.303RT/F$, leads to:

$$\left(\frac{\theta_R}{1-\theta_R}\right)^2 \exp(-2\times 2.303) = \frac{2k_a C_{H^+}\exp\left(-\alpha_a \frac{V_{R,a}F}{RT}\right)}{k_b}\exp(-2.303\alpha_a) \quad (28)$$

which directly rearranges to the following:

$$\frac{2k_a C_{H^+}\exp\left(-\alpha_a \frac{V_{R,a}F}{RT}\right)}{k_b} = \left(\frac{\theta_R}{1-\theta_R}\right)^2 10^{(-2+\alpha_a)} \quad (29)$$

which can be substituted into Eq. (23) to give:

$$\left(\frac{\theta}{1-\theta}\right)^2 = \left(\frac{\theta_R}{1-\theta_R}\right)^2 10^{(-2+\alpha_a)} \exp\left(-\alpha_a \frac{\eta F}{RT}\right) \quad (30)$$

Consequently by combination with Eq. (17), the hydrogen fugacity can be expressed by the following:

$$f_{H_2} = 10^{(-2+\alpha_a)} \exp\left(-\alpha_a \frac{\eta F}{RT}\right) \quad (31)$$

The slope of the Tafel curve through the region in which consumption of MH_{ads} occurs predominantly by reaction B is $RT/F\alpha_a$. At small values of overpotential, this equation does not directly apply as that is within the linear region where the reverse of reaction A is non-negligible. However, the trend of Eq. (31), as the overpotential approaches zero, is an intercept defined by $10^{\alpha_\alpha - 2}$. This is equal to $10^{-1.5}$ if α_a is equal to 0.5.

2.3 High values of overpotential

For the case of large overpotential, and for small change in θ with overpotential, the following condition is valid:

$$k_b \theta^2 \ll 2k_c C_{H^+} \theta \exp\left(-\alpha_c \frac{\eta F}{RT}\right) \quad (32)$$

The balance of rates of formation (Eq. (18)) of adsorbed hydrogen reduces to:

$$2k_a C_{H^+}(1-\theta)\exp\left(-\alpha_a \frac{VF}{RT}\right) = 2k_c C_{H^+} \theta \exp\left(-\alpha_c \frac{VF}{RT}\right) \quad (33)$$

Consequently, the overall system can be defined by:

$$\frac{\theta}{1-\theta} = \frac{k_a \exp\left(-\alpha_a \frac{VF}{RT}\right)}{k_c \exp\left(-\alpha_c \frac{VF}{RT}\right)} \quad (34)$$

This can be defined in terms of overpotential by:

$$\frac{\theta}{1-\theta} = \frac{k_a \exp\left(-\alpha_a \frac{F}{RT}[V_{R,a}+\eta]\right)}{k_c \exp\left(-\alpha_c \frac{F}{RT}[V_{R,c}+\eta]\right)} \quad (35)$$

which can be rearranged into a more transparent function for θ in Eq. (36) and for hydrogen fugacity in Eq. (37):

$$\frac{\theta}{1-\theta} = \frac{k_a}{k_c} \exp\left(\left[-\alpha_a V_{R,a} + \alpha_c V_{R,c}\right]\frac{F}{RT}\right) \exp\left(\left[-\alpha_a + \alpha_c\right]\frac{\eta F}{RT}\right) \quad (36)$$

$$f_{H_2} = \left(\frac{1-\theta_R}{\theta_R}\right)^2 \frac{{k_a}^2}{{k_c}^2} \exp\left(\left[-\alpha_a V_{R,a} + \alpha_c V_{R,c}\right]\frac{2F}{RT}\right) \exp\left(\left[-\alpha_a + \alpha_c\right]\frac{2\eta F}{RT}\right) \quad (37)$$

For the purposes of determining the pre-exponential, K_p is defined via:

$$K_p = \left(\frac{1-\theta_R}{\theta_R}\right)^2 \frac{{k_a}^2}{{k_c}^2} \exp\left(\left[-\alpha_a V_{R,a} + \alpha_c V_{R,c}\right]\frac{2F}{RT}\right) \quad (38)$$

which provides a revised equation for hydrogen fugacity:

$$f_{H_2} = K_p \exp\left(\left[-\alpha_a + \alpha_c\right]\frac{2\eta F}{RT}\right) \quad (39)$$

At the point of inflection between the two different Tafel slopes, defined by an inflection overpotential, η^*, the fugacities of hydrogen can be equated, resulting in:

$$K_p \exp\left(\left[-\alpha_a + \alpha_c\right]\frac{2\eta^* F}{RT}\right) = 10^{-2+\alpha_a} \exp\left(-\alpha_a \frac{\eta^* F}{RT}\right) \quad (40)$$

which allows determination of the constant K_p via:

$$K_p = 10^{-2+\alpha_a} \exp\left(\left[\alpha_a + 2\alpha_c\right]\frac{\eta^* F}{RT}\right) \quad (41)$$

which provides the following expression of hydrogen fugacity at large overpotentials:

$$f_{H_2} = 10^{-2+\alpha_a} \exp\left(\left[\alpha_a + 2\alpha_c\right]\frac{\eta^* F}{RT}\right) \exp\left(\frac{2[\alpha_c - \alpha_a]\eta F}{RT}\right) \quad (42)$$

As a direct consequence, for an overpotential such that reaction C can progress, if the charge transfer coefficients α_c and α_a are equal, then the fugacity of hydrogen does not increase further and is constant at higher overpotential, as determined by Bockris and Subramanyan [81]. However if α_c and α_a are not equal, the slope of the Tafel curve is defined by the difference between the two.

2.4 Conclusion

This theoretical analysis of the hydrogen evolution reaction provides an improved theoretical identification of the values of the parameters A and ζ in Eq. (3).

3. Experimental

3.1. Permeation tests

Hydrogen permeation in an annealed low interstitial steel (which was essentially pure iron) was studied using the Devanathan-Stachurski two-component electrolytic permeability cell [82] as illustrated in Fig. 2. Each compartment contained a Pt wire counter electrode, and a Luggin capillary probe connected to an Ag/AgCl reference electrode. The specimen was in the form of a flat sheet in the middle of the cell, and was the working electrode for each cell. The hydrogen input side was the left hand side, and the hydrogen permeating through the specimen was measured using the right hand cell. The steel composition is listed in Table 1. This steel can also be considered to be ultra low carbon steel, abbreviated as ULC steel. The steel was furnace annealed by heating at 700 °C for 3 hours, and furnace cooling. The low interstitial steel sheet exposed an area to the solution of 3.53 cm^2. The original sheet thickness was 1.0 mm. The samples were polished to different thicknesses for various experiments. The cathodic side of the specimen was polished to a mirror finish (3 μm diamond), washed with distilled water, washed with ethanol and dried.

To prevent oxidation, the anodic side was electrolytically Pd-plated, which coating was determined to be less than 1 μm in thickness, by weighing the specimen after the Pd plating. The solution used for Pd plating was 5 g $PdCl_2$ dissolved in 1 liter 25 wt% ammonia solution. The plating procedures were as follows. The specimen was (i) ground to 1200 grit emery paper on the Pd coating side, (ii) cleaned in an oil removal solution (NaOH 16 g, Na_2CO_3 15 g, $Na_3PO_4 \cdot 12H_2O$ 15 g, detergent 2 ml dissolved in 500 ml distilled water) at 80 °C for 15 min, (iii) washed with distilled water, (iv) dried by cool flowing air, (v) weighed, (vi) the polished input side was masked using an adhesive sticker, (vii) a conductive wire was connected to the specimen, (viii) the specimen was pickled for 5 s in 37 wt% HCl solution, (ix) washed thoroughly with distilled water, and (x) and the Pd was electro-deposited. The specimen was connected to the negative pole of the power supply, and a platinum electrode was connected with the positive pole of the power supply. The deposition lasted 5 min at a current density of 3 mA cm^{-2} in the solution of 5 g $PdCl_2$ in 1 L ammonia (25 wt%). The specimen was rinsed with ethanol, dried with cool flowing air, and weighed. The Pd coating was checked after each permeability transient sequence, and in no case was there detected any change.

The hydrogen charging solution in the left hand cell was either (i) 0.1M NaOH solution or (ii) the acidified pH 2 0.1M Na_2SO_4 solution as used in our prior research [42]. The hydrogen exit cell was filled with 0.1M NaOH solution (pH 12.6). All solutions were made from the analytic grade reagents and distilled water.

A MP81 potentiostat was used for hydrogen charging by controlling the cathodic potential. The hydrogen permeation current was recorded by anodically polarizing the hydrogen exit side to + 0.200 $V_{Ag/AgCl}$ using a PARSTAT 2273 potentiostat. The charging current density, i_c, was also measured for each charging condition.

Before each experiment, the exit side background current density was decreased to less than 0.2 μA cm^{-2} by N_2 bubbling through the solution. N_2 bubbling through the solution was continued throughout each experiment to continue to remove O_2 from the solution. Too high an O_2 concentration in the solution can contribute to the oxidation current density. All the tests were performed at room temperature, 23 ± 2 °C.

3.2. Permeation transients

For a specimen with a thickness of L, the hydrogen permeation transient can be expressed by the following equations [89, 118]:

$$\frac{i_t - i_o}{i_\infty - i_0} = \frac{2L}{\sqrt{\pi D t}} \sum_{n=0}^{\infty} \exp\left(-\frac{(2n+1)^2 L^2}{4Dt}\right), \quad \text{(rise transient)} \tag{43}$$

$$\frac{i_t - i_\infty}{i_0 - i_\infty} = 1 - \frac{2L}{\sqrt{\pi D t}} \sum_{n=0}^{\infty} exp\left(-\frac{(2n+1)^2 L^2}{4Dt}\right), \quad \text{(decay transient)} \tag{44}$$

where i_t is the measured hydrogen permeation current density at time t, i_0 is the initial steady-state hydrogen permeation current density at t = 0 from the prior transient, and $i_\infty$is the new steady-state hydrogen permeation current density as $t \rightarrow \infty$. In particular, for the first charging i_0 = 0, and for the complete decay i_∞ = 0. These two equations (Eq. (43) and Eq. (44)) were used to determine the diffusivity of hydrogen through the low interstitial steel membrane. MATLAB was used to fit each experimental permeation transient with the pertinent permeation equation, giving the diffusion coefficient D_H.

The concentration of hydrogen, C_H, at the subsurface on the hydrogen entry side was calculated using Eq. (7).

The hydrogen diffusivity was determined as the average value of the fitted values, D_H.

3.3 Experimental sequence

Initial experiments were carried out to study permeability transients with a virgin surface without pre-charging on the entry side. That is, the specimen surface was as-polished. Many such experiments were carried without pre-charging. The experimental results presented herein were carried out in the acidified pH 2 0.1M Na_2SO_4 solution. The successive transients presented in this work were measured at potentials: -0.600 $V_{Ag/AgCl}$, -0.650 $V_{Ag/AgCl}$, -0.700 $V_{Ag/AgCl}$, -1.400 $V_{Ag/AgCl}$, and -1.700 $V_{Ag/AgCl}$. These experiments with a virgin surface indicated unexpected behaviour that was hard to understand. There were transients that did not conform to Eq. (43) and Eq. (44), and behaviour that was not consistent with Eqs. (3) and (8). Nevertheless, some of these experiments were described herein to signpost potential problems.

Subsequent experiments were carried out with pre-charging on the entry side. Long-term cathodic polarisation at -1.500 $V_{Ag/AgCl}$ in 0.1 M NaOH solution was carried out over 140 h, interrupted to measure some permeation transients. The permeation current versus time was recorded. These permeation transients (such as -1.200 $V_{Ag/AgCl}$ to -1.500 $V_{Ag/AgCl}$, and then back to -1.200 $V_{Ag/AgCl}$) were measured after various charging times. When the permeation current achieved steady-state, i_∞, a successive transient was measured after changing the applied potential on the entry side. Depending on whether the potential was increased or decreased, a rise or decay transient marked the approach to the new steady state. These permeation transients conformed to Eq. (43) and Eq. (44).

Each permeation transient was analysed to give the diffusion coefficient, D and i_∞; which provided the critical data to allow evaluation of the sub-surface hydrogen concentration on the charging or input side of the specimen. Sufficient permeation transients were measured to ensure a consistent and precise measurement of D. The steady state amount of hydrogen in the measured permeation transient was related to the hydrogen solubility in the steel for the particular hydrogen charging conditions.

Successive permeation transients were measured at different potentials after 48 h uninterrupted cathodic polarisation at -1.500 $V_{Ag/AgCl}$. The successive potentials were -1.200 $V_{Ag/AgCl}$, -1.300 $V_{Ag/AgCl}$, -1.400 $V_{Ag/AgCl}$, -1.500 $V_{Ag/AgCl}$, -1.600 $V_{Ag/AgCl}$, -1.700 $V_{Ag/AgCl}$ and -1.800 $V_{Ag/AgCl}$.

Subsequently, analogous permeation experiments were carried out with pre-charging on the entry side at -1.400 $V_{Ag/AgCl}$ in the acidified pH 2 0.1M Na_2SO_4 solution.

4. Results - virgin surface

Many preliminary experiments were carried out using a virgin surface. The sample entry surfaces were still shiny after the experiments, indicating that there was no surface degradation from the hydrogen charging at the hydrogen entry side. Furthermore microscopic examination of the surface did not reveal any damage. There were no signs of cracks or blisters. Nevertheless, the permeation transients were not repeatable. There were unexpected phenomena. Three examples are presented in Fig. 3 to Fig. 5.

Fig. 3 illustrates the maximum current density phenomenon, as shown by the initial few transients in acidified pH 2 0.1M Na_2SO_4 solution. When the potential of -0.650 $V_{Ag/AgCl}$ was applied on the entry side of the specimen at P1, the current density, i_p, on the exit side, increased after several seconds equivalent to a breakthrough time. The permeation rate reached a maximum and then decreased slowly to a steady state value. There was similar behaviour when the potential was decreased to -0.700 $V_{Ag/AgCl}$ at P2. When the applied potential was increased at P3 to -0.650 $V_{Ag/AgCl}$, the permeation rate decreased to a minimum and subsequently increased. There was a similar behaviour when the potential was increased to -0.600 $V_{Ag/AgCl}$ at P4. Beck et al. [119] reported phenomena similar to the first transient in Fig. 3 in their experiments in 0.1N H_2SO_4 solution, which they attributed to the formation of irreversible hydrogen damage in the steel in the form of blisters, which they stated occurred for hydrogen charging conditions which exceeded a critical hydrogen concentration, C_K [119]. However, this explanation did not apply to the present experiments because (i) there was no sign of any damage visible on detailed microscopic examination of the specimen after the experiments, and (ii) there were reproducible well-behaved transients, as shown in Fig. 4, during the later part of the experimental sequence, which were measured after the measurements shown in Fig. 3 on the same specimen. A more likely explanation was that the behaviour shown in Fig. 3 was caused by some surface effects on the entry side of the specimen, such as the reduction of surface oxides/hydroxides.

Fig. 4 illustrates successive transients obtained from the potential loop from -0.600 $V_{Ag/AgCl}$ to -0.650 $V_{Ag/AgCl}$ and back to -0.600 $V_{Ag/AgCl}$. With increasing time, the steady-state permeation current density increased steadily for both rise transients and decay transients. The evaluated hydrogen diffusion coefficient was essentially constant with time, but the

increased steady state permeation rate indicated increasing hydrogen concentration at the surface of the specimen if evaluated according to Eq. (7), and indicated increasing hydrogen fugacity at the same applied potential, which was not consistent with Eq. (3). This behaviour is consistent with increasing real surface area due to the reduction of surface oxides/hydroxides during the experimental sequence.

Fig. 5 presents the transients at more negative potentials. The transients between -0.600 $V_{Ag/AgCl}$ to -0.650 $V_{Ag/AgCl}$ were consistent with Eq. (43) and Eq. (44). However, when the applied potential was changed from -0.650 $V_{Ag/AgCl}$ to -1.700 $V_{Ag/AgCl}$, the permeation current density, i_p, decreased instead of increasing. The steady state current densities at -1.700 $V_{Ag/AgCl}$ and -1.400 $V_{Ag/AgCl}$ were lower than those at -0.600 $V_{Ag/AgCl}$ and -0.650 $V_{Ag/AgCl}$. Eq. (3) indicates that more hydrogen is generated at a more negative potential [78], which would be expected to result in a higher steady-state permeation current density at a more negative potential. However, this was not the case for the transients to -1.700 $V_{Ag/AgCl}$ and -1.400 $V_{Ag/AgCl}$. The reason was not clear.

The experiments using a virgin surface presented unexpected behaviour that was hard to understand.

5. Results - 0.1M NaOH solution

5.1. Permeation transients

Fig. 6(a) presents the first measurements of the hydrogen permeation current density versus time of cathodic polarisation at -1.500 $V_{Ag/AgCl}$ at the input side for a low interstitial steel specimen in the 0.1 M NaOH solution. Within a few hours the permeation rate attained a near-steady value of about 2.5 µA cm^{-2}. However, thereafter the permeation rate increased until reaching a broad maximum at about 48 h. The maximum permeation rate was about 6 times higher than that for short-term polarisation. After 70 h, the permeation rate began to decrease slowly. Flis et al. [103] observed a similar trend of the permeation rate versus time. Fig. 6(b) presents typical data for the hydrogen permeation rate versus square root of the charging current density for the cathodic pre-charging polarisation at -1.500 $V_{Ag/AgCl}$ on the input side of an annealed low interstitial steel specimen (L = 0.88 mm) in 0.1 M NaOH solution. Fig. 6(c) presents corresponding typical data for the hydrogen charging current

density, i_c, versus charging time for cathodic pre-charging at -1.500 $V_{Ag/AgCl}$ on the input side of an annealed low interstitial steel specimen (L = 0.88 mm) in the 0.1 M NaOH solution. Figs. 6 (a), (b) and (c) indicate that both the hydrogen permeation current density, and the charging current density, increased during the cathodic polarisation at -1.500 $V_{Ag/AgCl}$ at the input side for a low interstitial steel specimen in the 0.1 M NaOH solution. This indicates that more hydrogen was produced at the input side of the permeability specimen (i.e. the speed of reaction (10) had probably increased and/or there had been an increase in the surface area on which this reaction occurred) and more hydrogen entered the steel. That is reaction (13) was also faster or more hydrogen entered the steel because the true surface area had increased. The line of best fit in Fig. 6(b) was as follows:

$$i_p = -24.32 + 11.91\sqrt{i_c} \qquad (45)$$

Fig. 7 presents typical hydrogen permeation curves (from -1.200 $V_{Ag/AgCl}$ to -1.500 $V_{Ag/AgCl}$) for the low interstitial steel specimen after various cathodic polarisation times at -1.500 $V_{Ag/AgCl}$ on the input side in the 0.1 M NaOH solution. These curves were measured together with those of Fig. 6(a), and showed the same trend as that in Fig. 6(a). The steady-state permeation current density increased with increasing cathodic polarisation time, and reached a maximum at about 46 h. Thereafter, the steady-state permeation current density remained at about the maximum value for at least 10 h, and subsequently decreased somewhat.

Previous research [79, 103, 120] has attributed such changes to the changed state of the steel surface which directly influenced the surface hydrogen concentration dissolved in the steel as follows: (i) the initial increase in the hydrogen permeation rate was attributed to both weak bonding of the adsorbed hydrogen (facilitating the transformation of H_{ads} to H_{abs}) and the increasing surface coverage (concomitant with a decrease in surface coverage by surface oxide/hydoxide) with increasing cathodic polarisation time, and (ii) the following decrease after 70 h hydrogen charging was attributed to the growth of an iron oxide deposit on the specimen surface despite the fact that the surface was cathodically polarised. (It was proposed that the evolving hydrogen could shield the steel surface so that the potential at the surface was much less cathodic than the applied potential).

These results indicated that 48 h cathodic polarisation produced a quasi-stable surface condition that was conducive to hydrogen entry so that the steady-state permeation rate

reached a maximum and remained in that condition for about 20 hours. This surface condition was quasi-stable and corresponded to the maximum hydrogen uptake by the low interstitial steel.

Transients were measured at different potentials after 48 h uninterrupted cathodic polarisation. Many successive transients were obtained, which showed good reproducible behaviour at the same cathodic potential. This agreed with the previous conclusion that after 48 h charging in alkaline solution, the surface condition on the entry side was in a relatively stable state.

Fig. 8 presents an example of permeation transients from -1.200 $V_{Ag/AgCl}$ to -1.800 $V_{Ag/AgCl}$ to -1.200 $V_{Ag/AgCl}$ with a step of -0.100 $V_{Ag/AgCl}$ at each potential change for a specimen with thickness L = 0.76 mm, measured after 48 h uninterrupted cathodic polarisation. The charging current density was measured for each charging condition, and was found to be a constant in each case. The permeation transients at different cathodic potentials were fitted to Eq. (43) and Eq. (44) to obtain the value of hydrogen diffusion coefficient, D_H. The value of C_H was evaluated using Eq. (7). Table 2 presents the values of D_H and C_H. The average value of D_H was $6.8 \pm 0.7 \times 10^{-5}$ cm^2 s^{-1}.

Fig. 9(a) presents the transients obtained after 48 h uninterrupted charging at -1.500 $V_{Ag/AgCl}$ from a thicker specimen, with thickness L = 0.88 mm, in the 0.1 M NaOH solution. The charging current density was measured for each charging condition, and was also found to be a constant in each case. Fig. 9(b) presents a typical fitting for a permeation rise transient by Matlab to Eq. (43) for the transient from -1.450 $V_{Ag/AgCl}$ to -1.650 $V_{Ag/AgCl}$ from the sequence of Fig. 9(a) for the low interstitial steel specimen in the 0.1 M NaOH solution after 48 h charging at -1.500 $V_{Ag/AgCl}$. Fig. 9(c) presents typical fitting for a permeation decay transient by Matlab to Eq. (44) for the transient from -1.850 $V_{Ag/AgCl}$ to -1.650 $V_{Ag/AgCl}$ from the sequence of Fig. 9(a) for the low interstitial steel specimen in the 0.1 M NaOH solution after 48 h charging at -1.500 $V_{Ag/AgCl}$. Fig. 9(d) presents the measured permeation rise transients from the sequence of Fig. 9(a) for the low interstitial steel specimen in the 0.1 M NaOH solution after 48 h charging at -1.500 $V_{Ag/AgCl}$. Also shown is the theoretical rise transient calculated with the average value of the diffusion coefficient. Figs. 9(b), (c) and (d) shows good fits of the data to the theoretical transients.

Table 3 presents the values of D_H and C_H for the specimen with a thickness of 0.88 mm. The average value of D_H was $6.4 \pm 0.7 \times 10^{-5}$ cm^2 s^{-1}, which was within experimental error of

the value obtained from the thinner specimen, 6.8 ± 0.7 × 10^{-5} cm^2 s^{-1}. This was in good agreement with literature [99, 104] values of the lattice diffusion of hydrogen in well-annealed pure iron of 7.5 ~8.0 × 10^{-5} cm^2 s^{-1}. The present data were slightly lower, especially at more positive potential, such as at -1.100 $V_{Ag/AgCl}$ and -1.200 $V_{Ag/AgCl}$. The explanation is that, even though the successive transient minimised hydrogen trapping [102, 104] by filling up the traps, there was nevertheless still some trapping. At a more positive potential, less hydrogen was generated, and due to the trapping, the apparent hydrogen diffusion coefficient was somewhat lower. This influence of trapping decreased with increasingly negative applied cathodic potential. At more negative potentials, many H atoms were generated, therefore, the trapped ones would have a lower influence on the evaluated lattice diffusion coefficient. At -1.700 $V_{Ag/AgCl}$, the average value was about 7.5 × 10^{-5} cm^2 s^{-1} (L = 0.76 mm), which can be considered as the real diffusivity of hydrogen in the low interstitial steel at room temperature. Similar values were measured with the thicker specimen, L = 0.88 mm.

The data related to the charging current density are presented in Figs. 10 and 11. Fig. 10 shows that the hydrogen solubility, C_H calculated using Eq. (7), increased approximately linearly with the square root of the charging current density, $\sqrt{i_c}$. This agreed with the theoretical expectation, and the results from other researchers [35, 79, 121]. Eq. (7), and the linear relationship in Fig. 10 between C_H and $\sqrt{i_c}$, indicated that the steady-state hydrogen permeation rate, $i_\infty \times L$, should be proportional to the $\sqrt{i_c}$, as was indeed the case, as presented in Fig. 11. The fitted line to the data of Fig. 11 was

$$i_\infty \times L = -0.20 + 0.45\sqrt{i_c}, \tag{46}$$

Fig. 12 presents the experimentally determined relationships between i_∞ and η from the two steel specimens. There was a turning point at about η = - 0.35 V. The relationship between $\ln i_\infty$ and η was linear both below and above this turning point. The slopes of each line were -5.94, -1.12 and -1.75, respectively, for *k1*, *k2* and *k3* in Fig. 12. Similar data were reported by Bockris et al. [79], which were also plotted in Fig. 12. They attributed the turning point at -1.02 V_{NHE} (η = - 0.275 V) to the change of mechanisms of hydrogen evolution. At lower overpotentials, the mechanism was considered to be the coupled discharge-recombination mechanism (the slope of the linear relationship of $\ln i_\infty$ and η (V), *K1*, was about -9.54); whereas at higher overpotentials, the mechanism was considered to have changed to a slow discharge-fast electrochemical mechanism (*K2*, about -1.74).

Fig. 13 presents the relationship between i_c and η. There was also a turning point, at about η = - 0.35 V, consistent with the data presented in Fig. 12. The fitting lines were as follows:

$$\ln i_c = -2.19 - 10.6\,\eta, |\eta| < 0.35\,V, \quad (47)$$

$$\ln i_c = 0.750 - 3.04\,\eta, \ |\eta| > 0.35\,V, \ (L = 0.76 \text{ mm}), \quad (48)$$

$$\ln i_c = 0.503 - 2.94\,\eta, |\eta| > 0.35\,V, (L = 0.88 \text{ mm}), \quad (49)$$

5.2. Hydrogen fugacity

Following the theoretical approach outlined above, the equivalence of electrochemical charging to gas phase charging was established from fitting the steady state permeability current to Eq. (9). Fig. 12 shows the determined relationship of between i_∞ and η. For low overpotential values, ($|\eta|$ < 0.35 V), $\frac{\partial \ln i_\infty}{\partial \eta} \approx -5.94$. Since F = 96485 C mol^{-1} and T = 296 K, ζ was calculated to be 3.30 according Eq. (9), and A was calculated to be 15.36 atm. The hydrogen fugacity could be expressed as:

$$f_{H_2} = 15.36 \exp\left(-\frac{\eta F}{3.30RT}\right), \text{ for } |\eta| < 0.35 \text{ V}. \quad (50)$$

At high overpotentials, i.e. $|\eta|$ > 0.35 V, there were data for two thicknesses. For L = 0.76 mm, $\frac{\partial \ln i_\infty}{\partial \eta} \approx -1.75$, then ζ and A were 11.20 and 443.7 atm, respectively. The hydrogen fugacity was given by:

$$f_{H_2} = 443.7 \exp\left(-\frac{\eta F}{11.20RT}\right). \quad (51)$$

For L = 0.88 mm, $\frac{\partial \ln i_\infty}{\partial \eta} \approx -1.12$, then ζ was 17.50 and A was 676.2 atm.

$$f_{H_2} = 676.2 \exp\left(-\frac{\eta F}{17.50RT}\right). \quad (52)$$

The differences in the fugacity values for the two thicknesses were attributed to slight differences in surface state on the input side of the low interstitial steel specimen. Figs. 6(a), (b) and (c) indicated that the pre-charging caused significant changes at the input side of the permeation specimen, and it is not unreasonable to expect slight differences in the surface state from specimen to specimen.

The average value was given by:

$$f_{H_2} = 560 \exp\left(-\frac{\eta F}{14.35RT}\right), \text{ for } |\eta| > 0.35 \text{ V} \quad (53)$$

Under the most severe charging condition in the 0.1 M NaOH solution, the calculated hydrogen fugacity, $\boldsymbol{f_{H_2}}$, according to Eq. (53) at an overpotential of 0.900 V was ~6 500 atm.

6. Results - 0.1M Na_2SO_4 solution

6.1. Permeation transients

Fig. 14 presents the hydrogen permeation current density versus time of hydrogen charging at -1.400 $V_{Ag/AgCl}$ at the entry side of the low interstitial steel permeability specimen in the acidified pH 2 0.1 M Na_2SO_4 solution. After ~10 hours charging, the permeation rate had become relatively stable at about 4.25 µA cm^{-2}. The spikes on the permeability current density of Fig. 14 represent the permeability measurements showed in Fig. 15.

Fig. 15 presents a typical transient loop after 21 h charging at -1.400 $V_{Ag/AgCl}$ at the entry side of the low interstitial steel permeability specimen. The trend was that the permeation current density increased with the increasingly negative potential at the entry side of the low interstitial steel permeability specimen. This was similar to that in the 0.1 M NaOH solution. The fitting values of D_H are listed in Table 4. C_H was evaluated using Eq. (7). The average value of D_H was 4.42 ± 0.4 × 10^{-5} cm^2 s^{-1}, almost half smaller than that ideal lattice diffusion coefficient. With charging time, the surface colour on the entry side changed from silver mirror to brown mirror to black. Therefore, the decrease in the D_H could have been caused by the changed surface condition. There might be a corrosion products layer on the surface during the long cathodic charging in the acidic solution [94]. There was no other feasible explanation as the specimen was the same steel as for the experiments in the 0.1M NaOH solution, the Pd coating on the exit side was the same, and the solution on the exit side was the same as previously. The only difference was on the entrance side of the specimen.

Fig. 16 and Fig. 17, respectively, show that there were again linear relationships between C_H or i_∞ and $\sqrt{i_c}$.

Fig. 18 presents the relationship between i_∞ and η for high overpotentials. The data of Fig. 18 extrapolated to low permeability current densities for low values of overpotential, so there did not appear to be a turning point for the permeability data in the acidified pH 2 0.1 M

Na_2SO_4 solution, in contrast to the data in the 0.1M NaOH solution shown in Fig. 12. There was a linear relationship between $\ln i_\infty$ and η, consistent with expectations from the theoretical evaluation described above. This could be expressed as follows.

$$\ln i_\infty = 0.086 - 1.19\,\eta \quad (54)$$

Fig. 19 indicated a linear relationship between $\ln i_c$ and η with the following line of best fit:

$$\ln i_c = -0.541 - 2.71\,\eta \quad (55)$$

6.2. Hydrogen fugacity

The hydrogen fugacity during electrolytic charging was evaluated from the relationship between i_∞ and η. According to Fig. 18, $\frac{\partial \ln i_\infty}{\partial \eta} = -1.19$, then ζ was 16.4 calculated using Eq. (9); and A was 10.9 atm. The hydrogen fugacity was given by:

$$f_{H_2} = 10.9 \exp\left(-\frac{\eta F}{16.47RT}\right) \quad (56)$$

Note that the hydrogen fugacity determined as Eq. (56) used the experimentally determined value of D_H as measured in the 0.1 M NaOH solution, rather than that determined in the acidified pH 2 0.1 M Na_2SO_4 solution, because it appears that the value determined in the acidified pH 2 0.1 M Na_2SO_4 solution was lower than it should be because of some surface impediment on the input side of the permeability specimen. The actual permeability inside the specimen was expected to be the same as for the permeability experiments in the 0.1M NaOH solution.

Under our most severe charging condition in the acidified pH 2 0.1 M Na_2SO_4 solution, the calculated hydrogen fugacity, $\boldsymbol{f_{H_2}}$, according to Eq. (56), was about 290 atm.

7. Discussion

7.1 Virgin surface

The experiments with the virgin surface showed that reproducible permeability transients were not produced, and moreover, there was no agreement with Eq. (3) using virgin low interstitial steel specimens in the acidified pH 2 0.1 M Na_2SO_4 solution; that is for specimens

that were not pre-charged for a substantial period of time. The transient behaviour was consistent with surface oxides/hydroxides causing impediment to hydrogen entry, and the amount of surface coverage to be changing with cathodic charging time due to the reduction of surface oxide/hydroxide. Since the charging condition was changing, the results obtained were unrepeatable. These effects were not studied in detail because reproducible results were obtained after long-term pre-charging was adopted.

7.2 Validity of approach

The approach presented herein to determine the hydrogen fugacity during electrolytic charging requires a number of conditions to be met. It is useful to consider these conditions.

Central to the approach is the Nernst equation, Eq. (3), which relates hydrogen fugacity to overpotential. The Nernst equation is a central thermodynamic foundation to electrochemical theory. The proper formulation of the form of the Nernst equation requires an understanding of the steps of the hydrogen evolution reaction given in Eqs. (10), (11) and (12).

The other major conditions are (i) that there is equilibrium between the hydrogen released by the electrochemical reaction at the steel surface, and the hydrogen dissolved in the steel at the steel surface, and that (ii) there are ideal permeation transients. Equilibrium is expected as the hydrogen is evolved at the metal surface, and so can easily enter into the steel. However, oxides (or other compounds) on the steel surface could cause surface impedance to the hydrogen entry. If these conditions are realised, then Eq. (8) indicates that the plot of $\ln i_\infty$and η is linear. In this research, the permeation transients presented in Figs. 8, 9 and 15 after prolonged charging where close to ideal transients in that they were well fitted to Eq. (43) and Eq. (44), see Fig. 9. Moreover, Fig. 12 indicated that, in each case, there was a turning point with increasing overpotential. Nevertheless, the plot of $\ln i_\infty$vs. η was linear both below and above the turning the point. The change in the slope of the $\ln i_\infty$vs. η line was ascribed to the change in the hydrogen evolution mechanism [79]. Furthermore, the prolonged pre-charging would be expected to reduce surface oxides to a stable condition.

In addition, the values of the diffusion coefficient listed in Table 2 and Table 3 were in good agreement with literature values for pure iron. These values were measured after prolonged hydrogen charging in the 0.1 M NaOH solution, and after repeated transients to fill up the existing hydrogen traps.

Thus, the experimental data indicated good compliance with the necessary conditions for applicability of the approach after prolonged hydrogen charging in the 0.1 M NaOH solution.

Compliance with the necessary conditions was also good after prolonged precharging in the acidified pH 2 0.1 M Na_2SO_4 solution, although the value of the measured diffusion coefficient was somewhat smaller, see Table 4. This was attributed to some surface impediment to hydrogen entry in this solution, and was confirmed by visual inspection of the sample surface aspect evolution during the permeation test. Once the hydrogen was inside the steel, permeation would have occurred as for the steel in the 0.1 M NaOH solution, and so the diffusion coefficient measured for the 0.1 M NaOH solution was used in the evaluation of the hydrogen fugacity relationship.

7.3 Theoretical evaluation

The data of Bockris et al. [79] in Figs. 12 and 20 suggest values for α_a and α_c of 0.4983 and 0.4537 respectively. The data from the present work, also presented in Figs. 12 and 20, suggest values for α_a and α_c of 0.3021 and 0.2673. This appears to be an entirely reasonable explanation for what occurred.

In general, the change in Tafel slope at overpotential values larger than the inflection overpotential η^*, implies an additional electrochemical reaction mechanism. It is clear from historical data that this can be explained by reaction C becoming active at large overpotentials, but having a smaller charge transfer coefficient than reaction A. The necessary difference is not large, and similar differences have been reported between overpotentials for the same reaction on different substrates [122]. In this case, the different substrate is the adsorbed hydrogen species instead of virgin metal.

There are no other readily apparent mechanisms to describe the change in Tafel slope. The exponential relation to overpotential implies an electrochemical component. Non-chemical reactions, or other behaviour hindering the reaction could reduce the slope of the curve, but would likely produce slopes that do not follow a consistent log-linear profile. Limitations of sites for reaction on the metal surface, caused by e.g. the formation of bubbles or other compounds providing a ‘catalytic-poisoning’ to the overall reaction mechanism would manifest as a limiting current and a transition from the Tafel slope toward that limiting current. Similarly transport-limited behaviours such as slow diffusion of hydrogen to the surface are unlikely to follow log-linear behaviour in response to an increase in overpotential.

The behaviour cannot be described by any reverse electrochemical reactions as their rates become negligible as the overpotential increases.

In terms of formation of other species on the surface, it cannot be explained by consumption of additional current / charge on formation of additional surface species, such as e.g. metal hydrogen complexes at different valence or metal-oxide-hydrogen complexes, as the formation of additional species would increase the slope of the relation between current and overpotential, which was not observed.

In this work there was a linear relationship between the steady state permeation current density, i_∞, and the square root of the current density of hydrogen evolution on the specimen surface, $\sqrt{i_c}$, see Figs. 6(b), 11 and 17. Similar relationships were measured by Bockris et al. [79]. This indicated that the measurements of the steady state permeation current density, i_∞, also provided information on the hydrogen evolution reaction that occurred on the input side on the permeability specimen. In particular, it was possible to say that there were no additional electrochemical reactions on the input surface of the permeability specimen. The reactions were comprised totally by (A), (B) and (C). Nevertheless, as also discussed above, there was also the transfer of hydrogen adsorbed atoms into the bulk of the steel by Eq.(13). Moreover, as discussed above, the surface state clearly had an influence as was evident from the somewhat different behaviour in the acidified pH 2 0.1 M Na_2SO_4 solution and in the 0.1M NaOH solution as is evident from a comparison of Figs. 12 and 18, and from Fig. 20. In addition, the true surface area of the specimen exposed to the solution can be different to the exposed surface area (because of surface coverage by oxides/hydroxides to a greater or lesser degree after cathodic charging), but this was not considered by Bockris and co-workers [79], [81]. But there was no significant amount of current associated with Fe oxidation, or the reduction of Fe oxides, or other conceivable side reactions.

7.4 Hydrogen fugacity

Fig. 20 presents the relationship of hydrogen fugacity with overpotential in the two solutions calculated according the above method: (i) in the 0.1M NaOH pH 12.6 solution given by Eqs. (50) and (53), and (ii) in the acidified pH 2 0.1M Na_2SO_4 solution given by Eq. (56). In each solution, at any overpotential value, there was some spread of the calculated values of fugacity as is clear from the data in Fig. 12. This spread is attributed to the accuracy of the evaluations of the fugacity, but may also be an inherent feature for steels as it is conceivable that there can be different true surface areas at a particular cathodic charging

condition. The relation for fugacity is an exponential function, and small errors in the evaluated value of ζ lead to large variations in the fugacity.

Fig. 20 also includes the fugacity evaluated from the results of Bockris et al. [79] given by Eqs. (15) and (16). That work by Bockris et al. [79] used a virgin surface, and their results were consistent with $\zeta = 2$, as expected from Bockris and Subramanyan [81] for the hydrogen evolution reaction by coupled electrochemical discharge-chemical recombination. In contrast, the results herein were obtained after significant precharging. The permeation currents were significantly larger, consistent with a higher hydrogen concentration, C_H, on the input side of the permeation specimen, and consistent with a higher hydrogen surface coverage because of less oxide on the surface. The calculated value of ζ herein was $\zeta = 3.30$ for the hydrogen fugacity in the 0.1M NaOH pH 12.6 solution. The higher value of ζ, or the lower value of the slope of i_∞ versus η in Fig. (12), is consistent with the higher hydrogen surface coverage allowing for some electrochemical hydrogen discharge by Eq. (12). It is also conceivable that the higher values of the permeation current density and the higher values of C_H, measured in this work compared with those of Bockris et al. [79] was due to some activated surface state as proposed by Bockris et al. [79].

The hydrogen fugacity developed in the experiments of Bockris et al [79] was lower than that developed in the present experiments. The actual fugacity developed can be related to the surface hydrogen coverage of the active surface sites. The results of Bockris et al. [79] are understandable by considering a modest hydrogen surface coverage, but a low hydrogen surface coverage of available sites, and there were relatively fewer available sites because a large number of the surface sites were blocked by surface oxide.

In this context, the research of Flis et al. [103] is relevant. They systematically studied the reasons for the significant increase in permeability current for iron after long time cathodic charging. They observed that atomic force microscopy (AFM) images of the iron surface after short time cathodic charging contained blurred images of the grinding marks. They attributed the blurred nature of the image to the air-formed surface oxides. After cathodic charging, particularly corresponding to the maximum of the permeability rate, the groves appeared sharp, attributed to the partial removal of oxides by cathodic reduction, and cathodic deposition of iron species. They maintained that sharpening of the grooves indicated an increase in the true surface area. They also postulated that there might be a change of

binding of the hydrogen to the surface of the metal, which it would seem would need to be reflected in a change in the hydrogen evolution energetics as proposed by Bockris et al. [79].

The data in Fig. 20 show that at the same overpotential, the hydrogen fugacity was higher in pH 12.6 solution than that in pH 2 solution. The difference may be due to the following two reasons.

The hydrogen adsorption mechanism is different in the two solutions. The hydrogen adsorption step may proceed through the following step in the acid (Eq. (57)) or alkaline solutions (Eq. (10)) [116]:

$$H_3O^+ + M + e \rightarrow M{\cdot}H_{ads} + H_2O \text{ (in acid solutions)} \quad (57)$$

These two reactions need different activation energies, leading to that even at the same overpotential, the reaction rates were different in the two solutions.

On the other hand, according to Pourbaix [95], SO_4^{2-} can be reduced to H_2S at negative potentials in the pH 2 solution. However, since negative potentials were applied on the sample, the double layer on the sample surface would be expected to consist of positive ions, like H_3O^+, instead of SO_4^{2-} ions, which would tend to aggregate at the counter electrode, where SO_4^{2-} ions were stable. Therefore, this is not considered as a reason for the different fugacity in two solutions.

The hydrogen fugacity in the two solutions can be influenced differently by the condition of the surface in each solution. The specimen surface subjected to long-term charging in the pH 12.6 solution was brown, while it was black in the pH 2 solution. This indicates that after long-term charging, both surface conditions were different from the original condition. Presumably, the changed surface, or the products precipitated on the surface, could influence the hydrogen absorption, and further influence the hydrogen fugacity under the entry subsurface of the membrane.

Nevertheless, the calculated hydrogen fugacity indicated that at the most severe charging condition (in the 0.1 M NaOH solution or in the acidified pH 2 0.1M Na_2SO_4 solution) the hydrogen fugacity was ~6 500 atm.

7.5 Alternative approaches

A substantial portion of the hydrogen embrittlement literature has employed hydrogen charging at constant current density [5, 7, 8, 16, 22, 27, 31, 34, 38, 48, 71, 72] rather than

constant potential [28, 51-53, 55, 57, 79]. As mentioned in the introduction, the Nernst equation is a relationship between the overpotential and the fugacity. It is more direct and clear to use potential charging than current density charging in this case. On the other hand, it is to some extent an issue to assign preference to control the potential rather than current. In any case, there is a relationship between the two. Potential has been considered as the primary controlling variable herein following Atrens et al. [78] based on [79-81].

7.6 Hydrogen embrittlement testing

What is the applicability to hydrogen embrittlement testing of the hydrogen fugacity values evaluated in Fig. 20 for conditions of static hydrogen entry in an electrolytic permeability cell? Hydrogen embrittlement testing is inherently slow, because it is necessary to allow sufficient time for the hydrogen to enter the steel, and to diffuse to the region where embrittlement occurs. Also it is not uncommon for there to be hydrogen precharging before the test to try to ensure a uniform hydrogen distribution at the start of the test. For example, our prior tests [42] involved pre-charging for 24 hours, and tests durations were from 1 to 4 days. Under such conditions, the present results are directly applicable.

Moreover, the dynamic straining inherent in the Linearly Increasing Stress Test (LIST) [42, 48, 50, 53, 54, 57, 61, 123] and the Constant Extension Rate Test (CERT) [35, 62, 67, 124] are likely to cause the rupture of any surface oxide films, causing direct access of the charging solution to the steel, and facilitating hydrogen entry into the steel. In particular, the long time pre-charging adopted herein was consistent with a higher surface area facilitating a greater amount of hydrogen in the steel surface. Similarly, LIST and CERT would also provide strain to break surface oxides and to expose un-oxidised steel directly to the charging conditions, and it would be expected that this would also lead to high hydrogen concentrations as measured herein due to the long time cathodic pre-charging.

These considerations mean that the hydrogen fugacity values of Fig. 20 are applicable to such hydrogen embrittlement testing. However, the values of hydrogen fugacity as determined herein by Eqs. (50), (53) and (56) are under-estimates because it is necessary to also consider the influence of stress on hydrogen solubility and diffusivity. The existing literature [101, 119, 125] indicates that an elastic stress increases the hydrogen solubility, and has no influence on the hydrogen diffusivity. This elastic stress state is the stress state to a first approximation in a LIST and a CERT until the onset of plasticity. Plastic strain can

cause hydrogen transport associated with the movement of dislocations [126-130] and can enhance hydrogen trapping [125, 126, 128-132].

7.7 Low interstitial steel

At the outset of this research, it was considered that the low interstitial steel (i.e. essentially pure iron) would be a good model material. There was the expectation that the hydrogen evolution reaction on the pure iron surface is essentially the same as on a steel surface. The results reported herein indicate that the hydrogen fugacity depends sensitively on the surface state. This means that it is not clear that the hydrogen fugacity on an alloy steel surface would be the same as measured herein on the low interstitial steel under similar circumstances. In addition, the quenched and tempered microstructure might provide a surface substantially different to the pure large-gained ferrite used herein. Experiments similar to those reported on herein are necessary using steel specimens. That research is beyond the scope of the present research.

7.8 Precharging

It is also worth noting that Fig. 20 shows that the hydrogen fugacity was different with or without precharging.

The use of a virgin surface led to irreproducible results in the research carried out herein, whereas Brockris et al. [79] measured reproducible permeation transients at low overpotentials, and also reported results consistent with those reported herein at high overpotential values. In contrast, the permeation transients were found herein to be reproducible after significant precharging. Moreover, long term precharging is more like that in a long term testing for the evaluation of hydrogen embrittlement using long term testing using LIST [42, 48, 50, 53, 54, 57, 61, 123] or CERT [35, 62, 67, 124].

7.9 Literature data

Fig. 21 shows the relationship between hydrogen fugacity (evaluated applying the above methodology to the data of Bockris et al. [79]) for pure iron for low values of overpotential in 0.1 N H_2SO_4 with various additions of KI. The hydrogen fugacity was evaluated to be:

$$f_{H_2} = 0.596 \exp\left(-\frac{\eta F}{2.16RT}\right), \text{ for no KI,} \tag{58}$$

$$f_{H_2} = 3.97 \exp\left(-\frac{\eta F}{2.42RT}\right), \text{ for } 10^{-4} \text{ M KI,} \tag{59}$$

$$f_{H_2} = 5.14 \exp\left(-\frac{\eta F}{2.23RT}\right), \text{ for } 5 \times 10^{-4} \text{ M KI,} \quad (60)$$

$$f_{H_2} = 44.5 \exp\left(-\frac{\eta F}{2.41RT}\right), \text{ for } 10^{-2} \text{ M KI,} \quad (61)$$

The Tafel slopes were essentially the same in each case, with $\zeta \sim 2$, consistent with hydrogen evolution largely by coupled electrochemical discharge-chemical recombination (i.e. coupled Eqs. (10) and (11)). The increasing magnitude of the fugacity with KI concentration is consistent with an increasing real surface area for the hydrogen evolution reaction. This is consistent with the fact that an increasing permeation current at any hydrogen evolution current was measured with increasing KI concentration. Alternatively there could be an increase in the equilibrium of Eq. (13), whereby there was a higher value of dissolved hydrogen for the same amount of adsorbed hydrogen in the presence of KI. In the acid solutions of low pH where iron oxides are not stable, this second explanation seems more likely, as was also suggested by Bockris et al. [79].

Fig. 22 shows the relationship between hydrogen fugacity (evaluated applying the above methodology to the data of Bockris et al. [79]) for pure iron in 0.1 M NaOH solution with various additions of KCN. The relationship for no KCN is given in Eqs. (15) and (16). In the presence of KCN, the hydrogen fugacity is given by:

$$f_{H_2} = 0.417 \exp\left(-\frac{\eta F}{2.82RT}\right), \text{ for } |\eta| < 0.35 \text{ V.} \quad (62)$$

$$f_{H_2} = 27.8 \exp\left(-\frac{\eta F}{17.1RT}\right), \text{ for } |\eta| > 0.35 \text{ V, and for } 1.6 \times 10^{-4} \text{ M KCN, and} \quad (63)$$

$$f_{H_2} = 14.0 \exp\left(-\frac{\eta F}{7.08RT}\right), \text{ for } |\eta| > 0.35 \text{ V, and for 0.1 M KCN.} \quad (64)$$

The data for low overpotential in terms of increasing fugacity are given by Eq. (15) for no KCN, Eq. (62) for KCN, and Eq. (50) for our data. These show increasing values of the pre-exponential factor A, and increasing values of ζ. This is consistent with increasing real surface area, and also a slight but increasing contribution from electrochemical desorption.

8. Conclusions

1. With a virgin surface, without precharging, there were irregular permeation transients, attributed to changing and irreproducible surface conditions.

2. Cathodic precharging conditioned the entry side of the low interstitial steel to a stable state, leading to reproducible permeability transients.
3. The hydrogen fugacity during electrochemical charging conditions was determined as Eqs. (50) and (53) for the 0.1 M NaOH solution, and as Eq. (56) for the acidified pH 2 0.1M Na_2SO_4 solution.
4. The lower slope of the hydrogen fugacity versus overpotential relationship at higher overpotentials in the 0.1 M NaOH solution is only explicable by different charge transfer coefficients for (i) the electrochemical discharge of hydrogen from a water molecule at the steel surface, and (ii) electrochemical desorption of a hydrogen atom adsorbed on the steel surface.
5. At the same overpotential, the hydrogen fugacity in the pH 12.6 solution was higher than that in pH 2 solution, attributed to differences in the hydrogen evolution reaction and differences in the surface state of the low interstitial steel in the two solutions.
6. Under the most severe charging condition, which was in the 0.1 M NaOH solution, the hydrogen fugacity was ~6 500 atm at an overpotential of 0.900 V.

List of symbols

f_{H_2}	hydrogen fugacity. The units are the same as those of pressure. The hydrogen fugacity is expressed herein in the units of atm.
A	constant in the equation relating hydrogen fugacity to overpotential, with units of atm.
F	Faraday
R	gas constant
T	absolute temperature
η	overpotential of the hydrogen evolution reaction
ζ	constant in the equation relating hydrogen fugacity to overpotential
E_H^0	equilibrium potential at the steel surface in the charging solution of the hydrogen evolution reaction at unit fugacity (i.e. at one atmosphere pressure).
E_c	applied potential
pH	acidity of the charging solution
pH 2	this solution had a pH value equal to 2.0
C_H	hydrogen concentration dissolved in the steel in equilibrium inside the steel sample.
S	Sievert's solubility constant
P_{H_2}	hydrogen pressure
i_∞	steady-state permeation current density at the exit side for a given negative potential at the entry side.
L	specimen thickness
D, D_H	hydrogen diffusion coefficient in the steel
${f_{H_2}}^e$	fugacity during electrolytic charging
MH_{ads}	a hydrogen atom adsorbed on the metal surface
MH_{abs}	a hydrogen atom absorbed on the metal surface
k_x, k_x'	forward and backward reaction rate constants in reactions (A), (B), and (C)
θ	proportion of surface sites occupied by MH_{ads} species
θ_R	surface hydrogen coverage at 1 atm pressure
t	time
C_{H^+}	concentration of hydrogen ions in solution

α_a	charge transfer coefficient of reaction (A)
α_c	charge transfer coefficient of reaction (C)
V	electrode potential
p_{H_2}	partial pressure of hydrogen
$V_{R,a}$	electrode potential constant for reaction (A) (defined in equation 23)
θ_{lin}	surface hydrogen coverage in region of linear relation between current density and overpotential
$V_{R,c}$	electrode potential constant for reaction (C) (defined in equations 34 & 35)
η^*	overpotential at inflection point between different Tafel slopes due to different reaction mechanisms for the hydrogen evolution reaction.
K_p	pre-exponential constant in relationship between fugacity and overpotential for overpotentials greater than η^*
i_t	measured hydrogen permeation current density at time *t*
i_0	initial steady-state hydrogen permeation current density at *t* = 0 from the prior transient
C_K	Critical hydrogen concentration above which irreversible hydrogen damage occurs
i_p	permeation current density
i_c	charging current density
$V_{Ag/AgCl}$	potential measured with respect to the Ag/AgCl electrode
V_{NHE}	potential measured with respect to the normal hydrogen electrode
k1, *k2*, *k3*, *K1*, *K2*	slopes in Fig. 12

9. Acknowledgement

This work is supported by an Australian Research Council linkage grant and Alstom (Switzerland) Ltd. The useful advice on the manuscript by Nick Winzer is gratefully acknowledged.

10.Reference

[1] E. Akiyama, K. Matsukado, M. Wang, K. Tsuzaki, Evaluation of hydrogen entry into high strength steel under atmospheric corrosion, Corrosion Science 52 (2010) 2758-2765.

[2] A. Alhussein, J. Capelle, J. Gilgert, S. Dominiak, Z. Azari, Influence of sandblasting and hydrogen on tensile and fatigue properties of pipeline API 5L X52 steel, International Journal of Hydrogen Energy 36 (2011) 2291-2301.

[3] L. Briottet, I. Moro, P. Lemoine, Quantifying the hydrogen embrittlement of pipeline steels for safety considerations, International Journal of Hydrogen Energy 37 (2012) 17616-17623.

[4] P. Castaño Rivera, V.P. Ramunni, P. Bruzzoni, Hydrogen trapping in an API 5L X60 steel, Corrosion Science 54 (2012) 106-118.

[5] E.V. Chatzidouros, V.J. Papazoglou, T.E. Tsiourva, D.I. Pantelis, Hydrogen effect on fracture toughness of pipeline steel welds, with in situ hydrogen charging, International Journal of Hydrogen Energy 36 (2011) 12626-12643.

[6] Y.S. Chun, J.S. Kim, K.-T. Park, Y.-K. Lee, C.S. Lee, Role of ε martensite in tensile properties and hydrogen degradation of high-Mn steels, Materials Science and Engineering: A 533 (2012) 87-95.

[7] C.F. Dong, Z.Y. Liu, X.G. Li, Y.F. Cheng, Effects of hydrogen-charging on the susceptibility of X100 pipeline steel to hydrogen-induced cracking, International Journal of Hydrogen Energy 34 (2009) 9879-9884.

[8] A.M. Elhoud, N.C. Renton, W.F. Deans, Hydrogen embrittlement of super duplex stainless steel in acid solution, International Journal of Hydrogen Energy 35 (2010) 6455-6464.

[9] D. Figueroa, M.J. Robinson, Hydrogen transport and embrittlement in 300 M and AerMet100 ultra high strength steels, Corrosion Science 52 (2010) 1593-1602.

[10] C.J.C. Filho, M.B. Mansur, P.J. Modenesi, B.M. Gonzalez, The effect of hydrogen release at room temperature on the ductility of steel wire rods for pre-stressed concrete, Materials Science and Engineering: A 527 (2010) 4947-4952.

[11] L.Q. Guo, Y. Bai, B.Z. Xu, W. Pan, J.X. Li, L.J. Qiao, Effect of hydrogen on pitting susceptibility of 2507 duplex stainless steel, Corrosion Science 70 (2013) 140-144.

[12] H.F. Jackson, C. San Marchi, D.K. Balch, B.P. Somerday, Effect of low temperature on hydrogen-assisted crack propagation in 304L/308L austenitic stainless steel fusion welds, Corrosion Science 77 (2013) 210-221.

[13] H. Je, A. Kimura, Stress corrosion cracking susceptibility of oxide dispersion strengthened ferritic steel in supercritical pressurized water dissolved with different hydrogen and oxygen contents, Corrosion Science 78 (2014) 193-199.

[14] J. Kittel, V. Smanio, M. Fregonese, L. Garnier, X. Lefebvre, Hydrogen induced cracking (HIC) testing of low alloy steel in sour environment: Impact of time of exposure on the extent of damage, Corrosion Science 52 (2010) 1386-1392.

[15] M. Koyama, E. Akiyama, T. Sawaguchi, K. Ogawa, I.V. Kireeva, Y.I. Chumlyakov, K. Tsuzaki, Hydrogen-assisted quasi-cleavage fracture in a single crystalline type 316 austenitic stainless steel, Corrosion Science 75 (2013) 345-353.

[16] M. Koyama, E. Akiyama, K. Tsuzaki, Hydrogen embrittlement in a Fe–Mn–C ternary twinning-induced plasticity steel, Corrosion Science 54 (2012) 1-4.

[17] A. Kuduzović, M.C. Poletti, C. Sommitsch, M. Domankova, S. Mitsche, R. Kienreich, Investigations into the delayed fracture susceptibility of 34CrNiMo6 steel, and the opportunities for its application in ultra-high-strength bolts and fasteners, Materials Science and Engineering: A 590 (2014) 66-73.

[18] L. Marchetti, E. Herms, P. Laghoutaris, J. Chêne, Hydrogen embrittlement susceptibility of tempered 9%Cr–1%Mo steel, International Journal of Hydrogen Energy 36 (2011) 15880-15887.

[19] T. Michler, J. Naumann, Hydrogen embrittlement of Cr-Mn-N-austenitic stainless steels, International Journal of Hydrogen Energy 35 (2010) 1485-1492.

[20] T. Michler, C. San Marchi, J. Naumann, S. Weber, M. Martin, Hydrogen environment embrittlement of stable austenitic steels, International Journal of Hydrogen Energy 37 (2012) 16231-16246.
[21] Y. Mine, K. Hirashita, M. Matsuda, M. Otsu, K. Takashima, Effect of hydrogen on tensile behaviour of micrometre-sized specimen fabricated from a metastable austenitic stainless steel, Corrosion Science 53 (2011) 529-533.
[22] A.P. Moon, R. Balasubramaniam, B. Panda, Hydrogen embrittlement of microalloyed rail steels, Materials Science and Engineering: A 527 (2010) 3259-3263.
[23] I. Moro, L. Briottet, P. Lemoine, E. Andrieu, C. Blanc, G. Odemer, Hydrogen embrittlement susceptibility of a high strength steel X80, Materials Science and Engineering: A 527 (2010) 7252-7260.
[24] D.N. Movchan, B.D. Shanina, V.G. Gavriljuk, Hydrogen effect on thermodynamic stability of γ- and ε-phases in a Fe–Cr–Mn solid solution, International Journal of Hydrogen Energy 38 (2013) 8471-8477.
[25] N.E. Nanninga, Y.S. Levy, E.S. Drexler, R.T. Condon, A.E. Stevenson, A.J. Slifka, Comparison of hydrogen embrittlement in three pipeline steels in high pressure gaseous hydrogen environments, Corrosion Science 59 (2012) 1-9.
[26] J. Naumann, T. Michler, Hydrogen environment embrittlement of orbital welded austenitic stainless steels at −50°C, International Journal of Hydrogen Energy 34 (2009) 6478-6483.
[27] S. Ningshen, U.K. Mudali, Hydrogen effects on pitting corrosion and semiconducting properties of nitrogen-containing type 316L stainless steel, Electrochimica Acta 54 (2009) 6374-6382.
[28] V. Olden, A. Alvaro, O.M. Akselsen, Hydrogen diffusion and hydrogen influenced critical stress intensity in an API X70 pipeline steel welded joint – Experiments and FE simulations, International Journal of Hydrogen Energy 37 (2012) 11474-11486.
[29] F.J. Recio, M.C. Alonso, L. Gaillet, M. Sánchez, Hydrogen embrittlement risk of high strength galvanized steel in contact with alkaline media, Corrosion Science 53 (2011) 2853-2860.
[30] F.J. Recio, Y. Wu, M.C. Alonso, U. Nürnberger, Hydrogen embrittlement risk in cold-drawn stainless steels, Materials Science and Engineering: A 564 (2013) 57-64.
[31] J. Rehrl, K. Mraczek, A. Pichler, E. Werner, Mechanical properties and fracture behavior of hydrogen charged AHSS/UHSS grades at high- and low strain rate tests, Materials Science and Engineering: A 590 (2014) 360-367.
[32] Q. Sha, D. Li, Microstructure, mechanical properties and hydrogen induced cracking susceptibility of X80 pipeline steel with reduced Mn content, Materials Science and Engineering: A 585 (2013) 214-221.
[33] J. Sojka, V. Vodárek, I. Schindler, C. Ly, M. Jérôme, P. Váňová, N. Ruscassier, A. Wenglorzová, Effect of hydrogen on the properties and fracture characteristics of TRIP 800 steels, Corrosion Science 53 (2011) 2575-2581.
[34] G. Wang, Y. Yan, J. Li, J. Huang, Y. Su, L. Qiao, Hydrogen embrittlement assessment of ultra-high strength steel 30CrMnSiNi2, Corrosion Science 77 (2013) 273-280.
[35] R. Wang, Effects of hydrogen on the fracture toughness of a X70 pipeline steel, Corrosion Science 51 (2009) 2803-2810.
[36] W.W. Wang, Y.J. Su, Y. Yan, J.X. Li, L.J. Qiao, W.Y. Chu, X.K. Wang, Y. Xing, The role of hydrogen in stress corrosion cracking of 310 austenitic stainless steel in a boiling MgCl2 solution, Corrosion Science 60 (2012) 275-279.
[37] Y. Wang, J. Gong, W. Jiang, A quantitative description on fracture toughness of steels in hydrogen gas, International Journal of Hydrogen Energy 38 (2013) 12503-12508.
[38] Y. Yao, L.J. Qiao, A.A. Volinsky, Hydrogen effects on stainless steel passive film fracture studied by nanoindentation, Corrosion Science 53 (2011) 2679-2683.

[39] A. Yonezu, T. Hara, T. Kondo, H. Hirakata, K. Minoshima, Evaluation of threshold stress intensity factor of hydrogen embrittlement cracking by indentation testing, Materials Science and Engineering: A 531 (2012) 147-154.
[40] C.M. Younes, A.M. Steele, J.A. Nicholson, C.J. Barnett, Influence of hydrogen content on the tensile properties and fracture of austenitic stainless steel welds, International Journal of Hydrogen Energy 38 (2013) 4864-4876.
[41] S. Zheng, Y. Qi, C. Chen, S. Li, Effect of hydrogen and inclusions on the tensile properties and fracture behaviour of A350LF2 steels after exposure to wet H2S environments, Corrosion Science 60 (2012) 59-68.
[42] Q. Liu, B. Irwanto, A. Atrens, The influence of hydrogen on 3.5NiCrMoV steel studied using the linearly increasing stress test, Corrosion Science 67 (2013) 193-203.
[43] S. Ramamurthy, A. Atrens, Stress corrosion cracking of high-strength steels, Corrosion Reviews 31 (2013) 1-31.
[44] D. Pérez Escobar, L. Duprez, A. Atrens, K. Verbeken, Thermal desorption spectroscopy study of experimental Ti/S containing steels, Materials Science and Technology 29 (2013) 261-267.
[45] D. Pérez Escobar, L. Duprez, A. Atrens, K. Verbeken, Influence of experimental parameters on Thermal Desorption Spectroscopy measurements during evaluation of hydrogen trapping, Journal of Nuclear Materials 450 (2014) 32-41.
[46] Q. Liu, A. Atrens, A critical review of the influence of hydrogen on the mechanical properties of medium-strength steels, Corrosion Reviews 31 (2013) 85-103.
[47] D. Pérez Escobar, E. Wallaert, L. Duprez, A. Atrens, K. Verbeken, Thermal desorption spectroscopy study of the interaction of hydrogen with TiC precipitates, Metals and Materials International 19 (2013) 741-748.
[48] S. Ramamurthy, W.M.L. Lau, A. Atrens, Influence of the applied stress rate on the stress corrosion cracking of 4340 and 3.5NiCrMoV steels under conditions of cathodic hydrogen charging, Corrosion Science 53 (2011) 2419-2429.
[49] W. Dietzel, A. Atrens, A. Barnoush. Mechanics of modern test methods and quantitative-accelerated testing for hydrogen embrittlement, in R.P. Gangloff and B.P. Somerday, Editors, Gaseous hydrogen embrittlement of materials in energy technologies, Woodhead, 2011: 237-273.
[50] S. Ramamurthy, A. Atrens, The influence of applied stress rate on the stress corrosion cracking of 4340 and 3.5NiCrMoV steels in distilled water at 30 °C, Corrosion Science 52 (2010) 1042-1051.
[51] E. Villalba, A. Atrens, Hydrogen embrittlement and rock bolt stress corrosion cracking, Engineering Failure Analysis 16 (2009) 164-175.
[52] E. Villalba, A. Atrens, Metallurgical aspects of rock bolt stress corrosion cracking, Materials Science and Engineering A 491 (2008) 8-18.
[53] E. Villalba, A. Atrens, SCC of commercial steels exposed to high hydrogen fugacity, Engineering Failure Analysis 15 (2008) 617-641.
[54] E. Villalba, A. Atrens, An evaluation of steels subjected to rock bolt SCC conditions, Engineering Failure Analysis 14 (2007) 1351-1393.
[55] E. Gamboa, A. Atrens, Material influence on the stress corrosion cracking of rock bolts, Engineering Failure Analysis 12 (2005) 201-235.
[56] E. Gamboa, A. Atrens, Stress corrosion cracking fracture mechanisms in rock bolts, Journal of materials science 38 (2003) 3813-3829.
[57] E. Gamboa, A. Atrens, Environmental influence on the stress corrosion cracking of rock bolts, Engineering Failure Analysis 10 (2003) 521-558.
[58] A. Oehlert, A. Atrens, Environmental assisted fracture for 4340 steel in water and air of various humidities, Journal of materials science 32 (1997) 6519-6523.
[59] Z. Wang, A. Atrens, Initiation of stress corrosion cracking for pipeline steels in a carbonate-bicarbonate solution, Metallurgical and Materials Transactions A 27 (1996) 2686-2691.

[60] A. Oehlert, A. Atrens, The initiation and propagation of stress corrosion cracking in AISI 4340 and 3.5 NiCrMoV rotor steel in constant load tests, Corrosion Science 38 (1996) 1159-1169.
[61] S. Ramamurthy, A. Atrens, The stress corrosion cracking of as-quenched 4340 and 3.5 NiCrMoV steels under stress rate control in distilled water at 90 C, Corrosion Science 34 (1993) 1385-1402.
[62] M. Wang, E. Akiyama, K. Tsuzaki, Effect of hydrogen on the fracture behavior of high strength steel during slow strain rate test, Corrosion Science 49 (2007) 4081-4097.
[63] A.J. West, M.R. Louthan, Hydrogen effects on the tensile properties of 21-6-9 stainless steel, Metallurgical and Materials Transactions A 13 (1982) 2049-2058.
[64] T. Depover, D. Pérez Escobar, E. Wallaert, Z. Zermout, K. Verbeken, Effect of hydrogen charging on the mechanical properties of advanced high strength steels, International Journal for Hydrogen Energy, 39 (2014) 4647–4656.
[65] D. Pérez Escobar, C. Minambres, L. Duprez, K. Verbeken, M. Verhaege, Internal and surface damage of multiphase steels and pure iron after electrochemical hydrogen charging, Corrosion Science 53 (2011) 3166-3176.
[66] D. Pérez Escobar, T. Depover, E. Wallaert, L. Duprez, M. Verhaege, K. Verbeken, Thermal desorption spectroscopy study of the interaction between hydrogen and different microstructural constituents in lab cast Fe-C alloys, Corrosion Science 65 (2012) 199-208.
[67] M. Wang, E. Akiyama, K. Tsuzaki, Effect of hydrogen and stress concentration on the notch tensile strength of AISI 4135 steel, Materials Science and Engineering A 398 (2005) 37-46.
[68] C.N. Panagopoulos, A.S. El-Amoush, K.G. Georgarakis, The effect of hydrogen charging on the mechanical behaviour of [alpha]-brass, Journal of Alloys and Compounds 392 (2005) 159-164.
[69] A. Glowacka, W.A. Swiatnicki, Effect of hydrogen charging on the microstructure evolution of duplex stainless steel, Materials Chemistry and Physics 81 (2003) 496-499.
[70] A. Glowacka, M.J. Wozniak, W.A. Swiatnicki, AFM study of austeno-ferritic stainless steel microstructure after cathodic hydrogen charging, Journal of Alloys and Compounds 404-406 (2005) 595-598.
[71] E. Herms, J.M. Olive, M. Puiggali, Hydrogen embrittlement of 316L type stainless steel, Materials Science and Engineering A 272 (1999) 279-283.
[72] C. Pan, Y.J. Su, W.Y. Chu, Z.B. Li, D.T. Liang, L.J. Qiao, Hydrogen embrittlement of weld metal of austenitic stainless steels, Corrosion Science 44 (2002) 1983-1993.
[73] D. Li, R. Gangloff, J. Scully, Hydrogen trap states in ultrahigh-strength AERMET 100 steel, Metallurgical and Materials Transactions A 35 (2004) 849-864.
[74] D. Hardie, J. Xu, E.A. Charles, Y. Wei, Hydrogen embrittlement of stainless steel overlay materials for hydrogenators, Corrosion Science 46 (2004) 3089-3100.
[75] E. Wallaert, T. Depover, M. Arafin, K. Verbeken, Thermal desorption spectroscopy of NbC and NbN precipitates, Metallurgical and Materials Transactions A, 45 (2014) 2412-2420.
[76] D. Pérez Escobar, T. Depover, L. Duprez, K. Verbeken, M. Verhaege, Combined thermal desorption spectroscopy, differential scanning calorimetry, scanning electron microscopy and X-ray diffraction study of hydrogen trapping in cold deformed TRIP steel, Acta Materialia 60 (2012) 2593-2605.
[77] D. Pérez Escobar, K. Verbeken, L. Duprez, M. Verhaege, Evaluation of hydrogen trapping in high strength steels by thermal desorption spectroscopy, Materials Science and Engineering: A 551 (2012) 50-58.
[78] A. Atrens, D. Mezzanotte, N.F. Fiore, M.A. Genshaw, Electrochemical studies of hydrogen diffusion and permeability in Ni, Corrosion Science 20 (1980) 673-684.
[79] J.O.M. Bockris, J. McBreen, L. Nanis, The Hydrogen Evolution Kinetics and Hydrogen Entry into a-Iron, Journal of The Electrochemical Society 112 (1965) 1025-1031.
[80] J. Bockris, A. Reddy. Modern Electrochemistry, 1970, Plenum Press, New York.

[81] J.O.M. Bockris, P.K. Subramanyan, The equivalent pressure of molecular hydrogen in cavities within metals in terms of the overpotential developed during the evolution of hydrogen, Electrochimica Acta 16 (1971) 2169-2179.
[82] M.A.V. Devanathan, Z. Stachurski, The Adsorption and Diffusion of Electrolytic Hydrogen in Palladium, Proceedings of the Royal Society of London. Series A. Mathematical and Physical Sciences 270 (1962) 90-102.
[83] H. Addach, P. Berçot, M. Rezrazi, J. Takadoum, Study of the electrochemical permeation of hydrogen in iron, Corrosion Science 51 (2009) 263-267.
[84] N. Boes, H. Züchner, Electrochemical methods for studying diffusion, permeation and solubility of hydrogen in metals, Journal of the Less Common Metals 49 (1976) 223-240.
[85] J. Choi, Diffusion of hydrogen in iron, Metallurgical Transactions 1 (1970) 911-919.
[86] H.J. Grabke, E. Riecke, Absorption and diffusion of hydrogen in steels, Materiali in Tehnologije 34 (2000) 331-342.
[87] M. Hashimoto, R. Latanision, Experimental study of hydrogen transport during plastic deformation in iron, Metallurgical and Materials Transactions A 19 (1988) 2789-2798.
[88] R.A. Oriani, The diffusion and trapping of hydrogen in steel, Acta Metallurgica 18 (1970) 147-157.
[89] E. Owczarek, T. Zakroczymski, Hydrogen transport in a duplex stainless steel, Acta Materialia 48 (2000) 3059-3070.
[90] X. Sun, J. Xu, Y. Li, Hydrogen permeation behavior in metastable austenitic stainless steels 321 and 304, Acta Metallurgica 37 (1989) 2171-2176.
[91] J. Vökl, H. Wipf, Diffusion of hydrogen in metals, Hyperfine Interactions 8 (1981) 631-637.
[92] S. Wach, A.P. Miodownik, J. Mackowiak, The diffusion of hydrogen through pure iron membranes, Corrosion Science 6 (1966) 271-285.
[93] D.A. Jones, Principles and prevention of corrosion, Pentice Hall, 1992.
[94] H. Kaesche, Metallic Corrosion, NACE, 1985.
[95] M. Pourbaix, Atlas of electrochemical equilibria in aqueous solutions, Pergamon Press, 1966.
[96] P. Marcus, ed. Corrosion mechanisms in theory and practice. 2 ed, New York: Marcel Dekker, 2002.
[97] P. Delahay, M. Pourbaix, P. Van Rysselberghe, Potential-pH diagrams, Journal of Chemical Education 27 (1950) 683.
[98] C.E.J. Holley, W.J. Worlton, R.K. Zeigler. Compressibility factors and fugacity coefficients calculated from the beattie-bridgeman equation of state for hydrogen, nitrogen, oxygen, carbon dioxide, ammonia, methane, and helium. Report: LA-2271 Los Alamos Scientific Lab, 1958.
[99] K. Kiuchi, R.B. McLellan, The solubility and diffusivity of hydrogen in well-annealed and deformed iron, Acta Metallurgica 31 (1983) 961-984.
[100] S.I. Sandler, Chemical, biochemical and engineering thermodynamics, 4th ed, John Wiley & Sons, New York, 2006.
[101] U. Hadam, T. Zakroczymski, Absorption of hydrogen in tensile strained iron and high-carbon steel studied by electrochemical permeation and desorption techniques, International Journal of Hydrogen Energy 34 (2009) 2449-2459.
[102] T. Zakroczymski, Z. Szklarska‐Smialowska, Activation of the Iron Surface to Hydrogen Absorption Resulting from a Long Cathodic Treatment in NaOH Solution, Journal of The Electrochemical Society 132 (1985) 2548-2552.
[103] J. Flis, T. Zakroczymski, V. Kleshnya, T. Kobiela, R. Duś, Changes in hydrogen entry rate and in surface of iron during cathodic polarisation in alkaline solutions, Electrochimica Acta 44 (1999) 3989-3997.
[104] T. Zakroczymski, Adaptation of the electrochemical permeation technique for studying entry, transport and trapping of hydrogen in metals, Electrochimica Acta 51 (2006) 2261-2266.

[105] I. Flis-Kabulska, J. Flis, T. Zakroczymski, Promotion of hydrogen entry into iron from NaOH solution by iron–oxygen species, Electrochimica Acta 52 (2007) 7158-7165.
[106] I. Flis-Kabulska, T. Zakroczymski, J. Flis, Accelerated entry of hydrogen into iron from NaOH solutions at low cathodic and low anodic polarisations, Electrochimica Acta 52 (2007) 2966-2977.
[107] I. Flis-Kabulska, J. Flis, T. Zakroczymski, Enhanced hydrogen entry into iron from 0.1 M NaOH at definite potentials, Electrochimica Acta 53 (2008) 3094-3101.
[108] M. Aoki, H. Saito, M. Mori, Y. Ishida, M. Nagumo, Deformation microstructures of a low carbon steel characterized by tritium autoradiography and thermal desorption spectroscopy, Journal of the Japan Institute of Metals-Nihon Kinzoku Gakkaishi 58 (1994) 1141-1148.
[109] T.-C. Lin, G. Seshadri, J.A. Kelber, A consistent method for quantitative XPS peak analysis of thin oxide films on clean polycrystalline iron surfaces, Applied surface science 119 (1997) 83-92.
[110] H. Mathieu, M. Datta, D. Landolt, Thickness of natural oxide films determined by AES and XPS with/without sputtering, Journal of Vacuum Science & Technology A: Vacuum, Surfaces, and Films 3 (1985) 331-335.
[111] P. Graat, M.A. Somers, Quantitative analysis of overlapping XPS peaks by spectrum reconstruction: determination of the thickness and composition of thin iron oxide films, Surface and interface analysis 26 (1998) 773-782.
[112] M. Aronniemi, J. Lahtinen, P. Hautojärvi, Characterization of iron oxide thin films, Surface and interface analysis 36 (2004) 1004-1006.
[113] W. Beck, J. Bockris, M. Genshaw, P. Subramanyan, Diffusivity and solubility of hydrogen as a function of composition in Fe-Ni alloys, Metallurgical and Materials Transactions B 2 (1971) 883-888.
[114] J.M. Bockris, M.A. Genshaw, M. Fullenwider, The electro-permeation of hydrogen into metals, Electrochimica Acta 15 (1970) 47-60.
[115] J. McBreen, M.A. Genshaw, In Fundamental Aspects of Stress Corrosion Cracking. R.W. Staehle, A.J. Forty, and D.v. Rooyens (Eds), NACE, (1967).p. 51-63.
[116] A. Lasia, D. Gregoire, General Model of Electrochemical Hydrogen Absorption into Metals, Journal of The Electrochemical Society 142 (1995) 3393-3399.
[117] O. Levenspiel, Chemical reaction engineering, 3 ed, McGraw-Hill Higher Education, New York, 1999.
[118] J. McBreen, L. Nonis, W. Beck, A Method for Determination of the Permeation Rate of Hydrogen Through Metal Membranes, Journal of The Electrochemical Society 113 (1966) 1218-1222.
[119] W.Beck, J.O.M. Bockris, J. McBreen, L. Nanis, Hydrogen permeation in metals as a function of stress temperature and dissolved hydrogen concentration, Proceedings of the royal society of london series a-mathematical and physical sciences 290 (1966) 220-235.
[120] C.D. Kim, B.E. Wilde, The Kinetics of Hydrogen Absorption into Iron during Cathodic Hydrogen Evolution, Journal of The Electrochemical Society 118 (1971) 202-206.
[121] M. Yan, Y. Weng, Study on hydrogen absorption of pipeline steel under cathodic charging, Corrosion Science 48 (2006) 432-444.
[122] B.K. n.d. Lecture 9: Evans Diagrams, Corrosion and Electrochemistry, Institute of Corrosion and Multiphase Technology, Ohio University, 2013.
[123] A. Atrens, C. Brosnan, S. Ramamurthy, A. Oehlert, I. Smith, Linearly increasing stress test (LIST) for SCC research, Measurement Science and Technology 4 (1993) 1281-1292.
[124] N. Winzer, A. Atrens, W. Dietzel, G. Song, K. Kainer, Comparison of the linearly increasing stress test and the constant extension rate test in the evaluation of transgranular stress corrosion cracking of magnesium, Materials Science and Engineering A 472 (2008) 97-106.
[125] Y. Huang, A. Nakajima, A. Nishikata, T. Tsuru, Effect of mechanical deformation on permeation of hydrogen in iron, ISIJ International 43 (2003) 548-554.

[126] K.-T. Kim, S.-I. Pyun, Hydrogen permeation through 3.3Ni 1.6Cr steel during plastic deformation, Scripta Metallurgica 22 (1988) 1719-1723.
[127] G. Frankel, R. Latanision, Hydrogen transport during deformation in nickel: Part I. Polycrystalline nickel, Metallurgical and Materials Transactions A 17 (1986) 861-867.
[128] I.-W. Kang, S.-I. Pyun, K.-T. Kim, The effects of dislocations on the trapping and transport of hydrogen in 3.3 Ni - 1.6 Cr steel during plastic deformation, Scripta Metallurgica 23 (1989) 223-226.
[129] A.M. Brass, J. Chene, Influence of deformation on the hydrogen behavior in iron and nickel base alloys: a review of experimental data, Materials Science and Engineering: A 242 (1998) 210-221.
[130] A.M. Brass, J. Chêne, Influence of tensile straining on the permeation of hydrogen in low alloy Cr–Mo steels, Corrosion Science 48 (2006) 481-497.
[131] S.J. Kim, H.G. Jung, K.Y. Kim, Effect of tensile stress in elastic and plastic range on hydrogen permeation of high-strength steel in sour environment, Electrochimica Acta 78 (2012) 139-146.
[132] M. Kurkela, G.S. Frankel, R.M. Latanision, S. Suresh, R.O. Ritchie, Influence of plastic deformation on hydrogen transport in 2 14 Cr-1Mo steel, Scripta Metallurgica 16 (1982) 455-459.

Table 1 Chemical composition of the low interstitial steel (wt%).

Sample	C	Mn	Si	S	P	Ni	Cr	Mo	Cu	V	Nb	Ti	Al	B	Fe
steel	0.005	0.043	<0.01	<0.005	0.005	0.012	0.013	<0.005	0.005	<0.005	<0.005	<0.005	<0.005	<0.0002	Bal

Table 2 D_H and C_H values for the low interstitial steel from permeability experiments such as those illustrated in Fig. 7 using a charging solution of 0.1M NaOH solution, L = 0.76 mm, F = 96485 C mol^{-1}, T = 296 K. Permeability transients were started after charging at -1.500 $V_{Ag/AgCl}$ for 48 h.

Potential, $V_{Ag/AgCl}$	Overpotential, V	i_∞, μA cm^{-2}	D, cm^2 s^{-1}	C_H, mol m^{-3}
-1.300	-0.3563	9.67	5.66×10^{-5}	0.135
-1.400	-0.4563	14.48	6.87×10^{-5}	0.166
-1.500	-0.5563	18.79	7.04×10^{-5}	0.210
-1.600	-0.6563	23.00	7.09×10^{-5}	0.256
-1.700	-0.7563	27.04	7.60×10^{-5}	0.280
-1.800	-0.8563	30.27	6.78×10^{-5}	0.352
-1.700	-0.7563	26.88	7.42×10^{-5}	0.286
-1.600	-0.6563	22.98	7.68×10^{-5}	0.236
-1.500	-0.5563	18.86	6.93×10^{-5}	0.214
-1.400	-0.4563	14.02	6.49×10^{-5}	0.170
-1.300	-0.3563	9.32	6.75×10^{-5}	0.109
-1.200	-0.2563	5.21	5.72×10^{-5}	0.072
		Average	$6.8 \pm 0.7 \times 10^{-5}$	

Table 3 D_H and C_H values for the low interstitial steel from permeability experiments such as those illustrated in Fig. 8 using a charging solution of 0.1M NaOH solution, L = 0.88 mm, F = 96485 C mol^{-1}, T = 296 K. Permeability experiments were started after charging at -1.500 $V_{Ag/AgCl}$ for 48 h.

Potential, $V_{Ag/AgCl}$	i_∞, μA cm^{-2}	D, cm^2 s^{-1}	C_H, mol m^{-3}
-1.100	2.90	5.23×10^{-5}	0.0505
-1.100	2.86	5.24×10^{-5}	0.0497
-1.100	2.99	5.42×10^{-5}	0.0503
-1.250	7.50	5.29×10^{-5}	0.1294
-1.250	7.31	6.67×10^{-5}	0.0998
-1.250	7.45	5.29×10^{-5}	0.1286
-1.250	7.29	6.40×10^{-5}	0.1039
-1.250	7.71	5.60×10^{-5}	0.1255
-1.250	7.47	6.51×10^{-5}	0.1046
-1.450	11.97	6.54×10^{-5}	0.1669
-1.450	11.87	6.61×10^{-5}	0.1637
-1.450	12.01	6.45×10^{-5}	0.1699
-1.450	11.94	6.90×10^{-5}	0.1577
-1.450	12.20	6.19×10^{-5}	0.1798
-1.450	12.22	6.56×10^{-5}	0.1699
-1.650	15.56	6.51×10^{-5}	0.2182
-1.650	15.48	7.24×10^{-5}	0.1949
-1.650	15.44	7.07×10^{-5}	0.1992
-1.650	15.75	7.14×10^{-5}	0.2012
-1.650	16.01	7.08×10^{-5}	0.2062
-1.650	15.82	6.73×10^{-5}	0.2145
-1.850	18.54	6.32×10^{-5}	0.2677
-1.850	17.89	7.86×10^{-5}	0.2077
-1.850	18.95	6.81×10^{-5}	0.2537
		Average $6.4 \pm 0.7 \times 10^{-5}$	

Table 4 D_H and C_H values for the low interstitial steel from permeability experiments such as those illustrated in Fig. 15 using a charging solution of acidified pH 2 0.1M Na_2SO_4 solution, L = 0.75 mm, F = 96485 C mol^{-1}, T = 296 K. Permeability experiments were started after charging at -1.400 $V_{Ag/AgCl}$ for 48 h.

Potential, $V_{Ag/AgCl}$	i_∞, μA cm^{-2}	D, cm^2 s^{-1}	C_H, mol m^{-3}
-1.200	9.30	4.61×10^{-5}	4.45×10^{-2}
-1.200	9.26	4.67×10^{-5}	4.37×10^{-2}
-1.200	9.31	4.80×10^{-5}	4.27×10^{-2}
-1.200	9.16	4.71×10^{-5}	4.29×10^{-2}
-1.200	9.30	4.84×10^{-5}	4.23×10^{-2}
-1.200	9.26	4.95×10^{-5}	4.12×10^{-2}
-1.200	9.22	4.59×10^{-5}	4.42×10^{-2}
-1.200	9.16	4.69×10^{-5}	4.30×10^{-2}
-1.200	9.16	4.64×10^{-5}	4.35×10^{-2}
-1.200	9.07	4.48×10^{-5}	4.46×10^{-2}
-1.400	13.82	3.82×10^{-5}	7.96×10^{-2}
-1.400	13.65	4.08×10^{-5}	7.37×10^{-2}
-1.500	16.05	4.02×10^{-5}	8.78×10^{-2}
-1.500	15.92	4.17×10^{-5}	8.40×10^{-2}
-1.600	18.11	4.26×10^{-5}	9.37×10^{-2}
-1.600	18.06	4.34×10^{-5}	9.16×10^{-2}
-1.600	17.99	4.26×10^{-5}	9.29×10^{-2}
-1.700	19.86	4.01×10^{-5}	1.09×10^{-1}
-1.700	19.65	4.24×10^{-5}	1.02×10^{-1}
-1.700	19.61	4.24×10^{-5}	1.02×10^{-1}
		Average $4.4 \pm 0.4 \times 10^{-5}$	

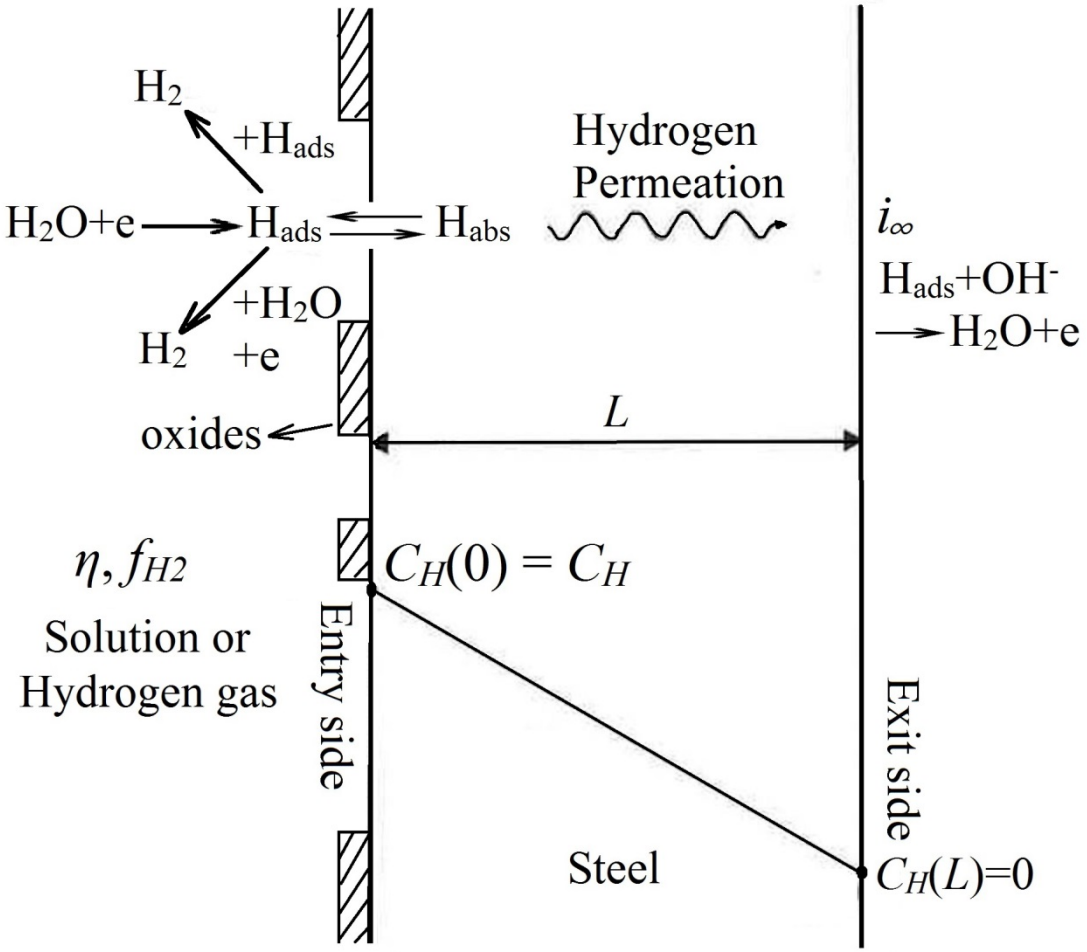

Fig. 1 Schematic showing the conditions at steady state for an ideal permeability specimen in an ideal experiment. The hydrogen conditions on the surface of the entry side of a permeability specimens (on the left hand side of the specimen) are given by a balance of the steps of the hydrogen evolution reaction, given by Eqs. (10), (11) and (12), and how these are influenced by the solution, the overpotential, and the state of the surface, including the presence of surface oxides and hydroxides, which tend to be reduced at cathodic potentials. The hydrogen adsorbed on the surface, H_{ads}, is in equilibrium with the hydrogen absorbed in solid solution just inside the permeability specimen, $H_{abs,}$ which determines the hydrogen concentration, C_H. The hydrogen diffuses through the permeability specimen, and the amount exiting on the right hand side of the specimen is measured as an electric current density. Adapted from [96].

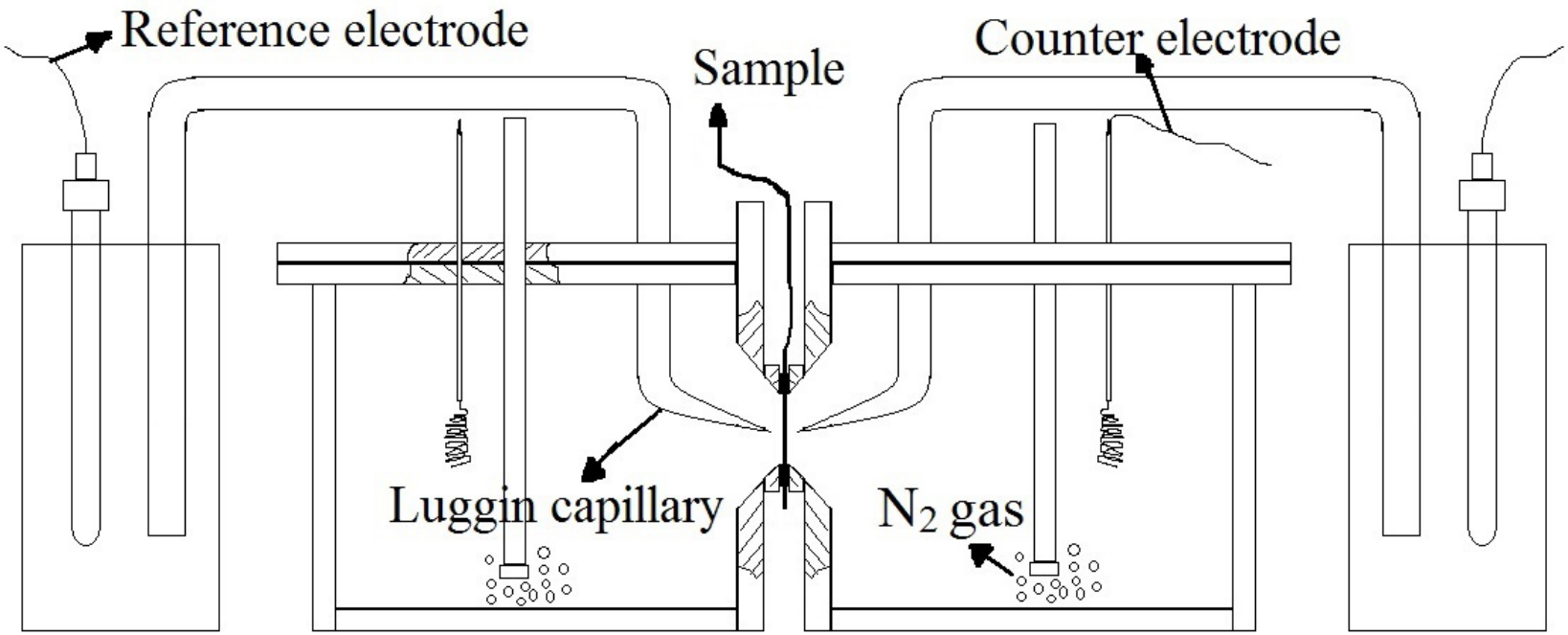

Fig. 2 Schematic of the electrolytic permeability cell.

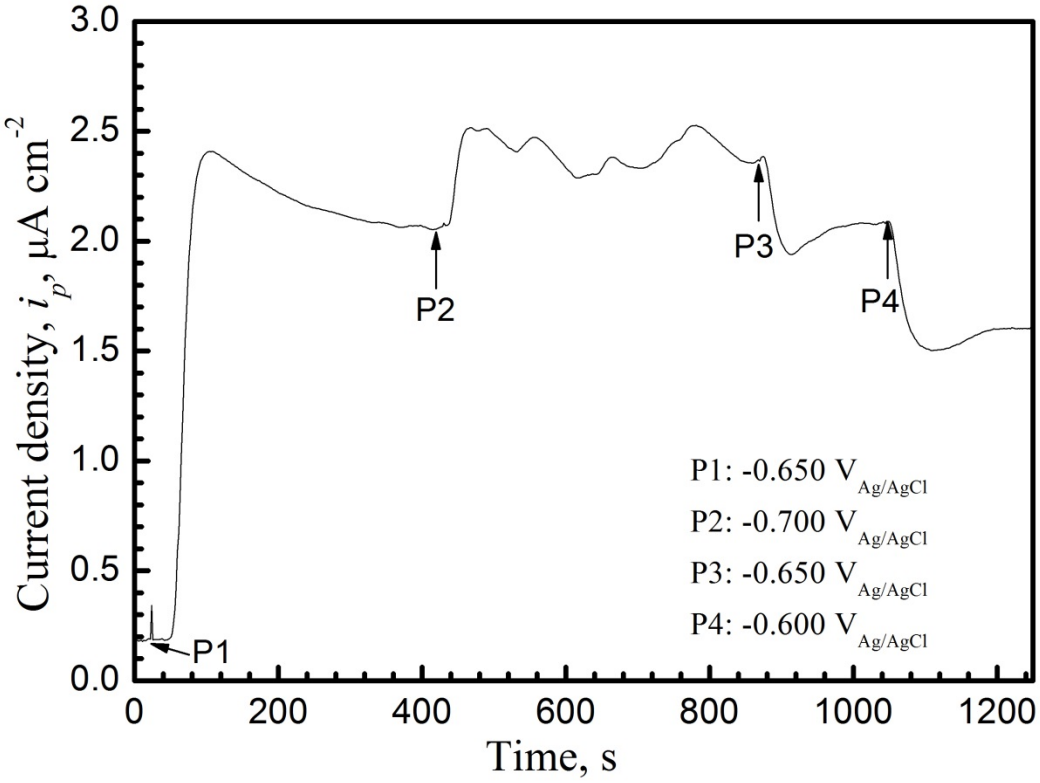

Fig. 3 Initial permeation transients for the low interstitial steel in acidified pH 2 0.1M Na_2SO_4 solution. The current density versus time is presented. The potential on the input side of the low interstitial steel membrane was set to -0.650 $V_{Ag/AgCl}$ at P1, to -0.700 $V_{Ag/AgCl}$ at P2, to -0.650 $V_{Ag/AgCl}$ at P3, and set to -0.600 $V_{Ag/AgCl}$ at P4.

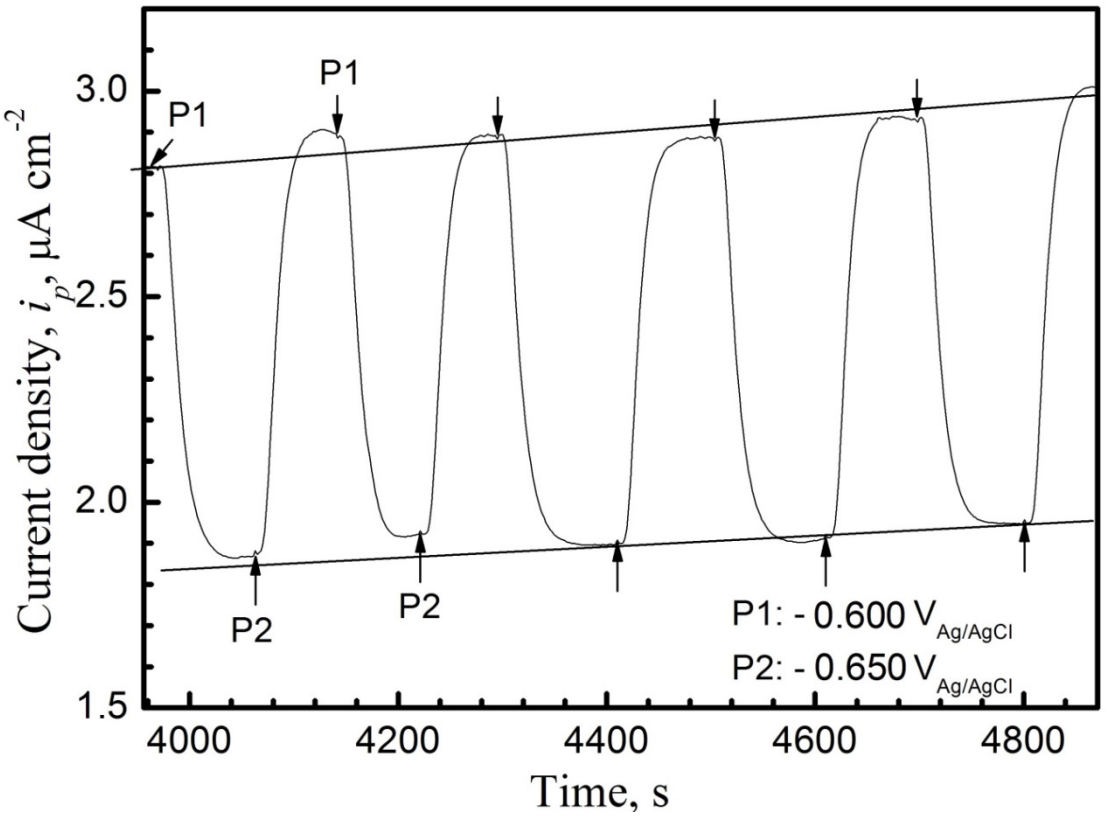

Fig. 4 Successive transients obtained for the low interstitial steel in acidified pH 2 0.1M Na_2SO_4 solution. The potential on the input side of the low interstitial steel membrane was set to -0.600 $V_{Ag/AgCl}$ at P1, and set to -0.650 $V_{Ag/AgCl}$ at P2.

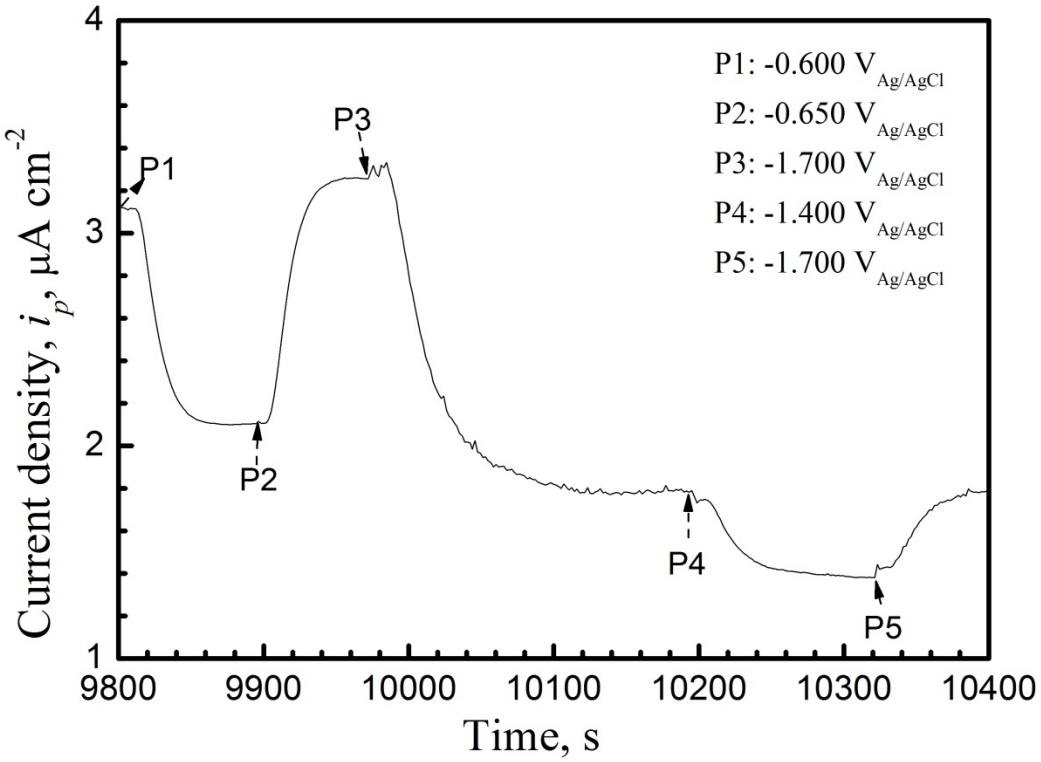

Fig. 5 Transients obtained in the acidified pH 2 0.1M Na_2SO_4 solution at more negative potentials. The potential on the input side of the low interstitial steel membrane was set to -0.600 $V_{Ag/AgCl}$ at P1, to -0.650 $V_{Ag/AgCl}$ at P2, to -1.700 $V_{Ag/AgCl}$ at P3, to -1.400 $V_{Ag/AgCl}$ at P4, and to -1.700 $V_{Ag/AgCl}$ at P5.

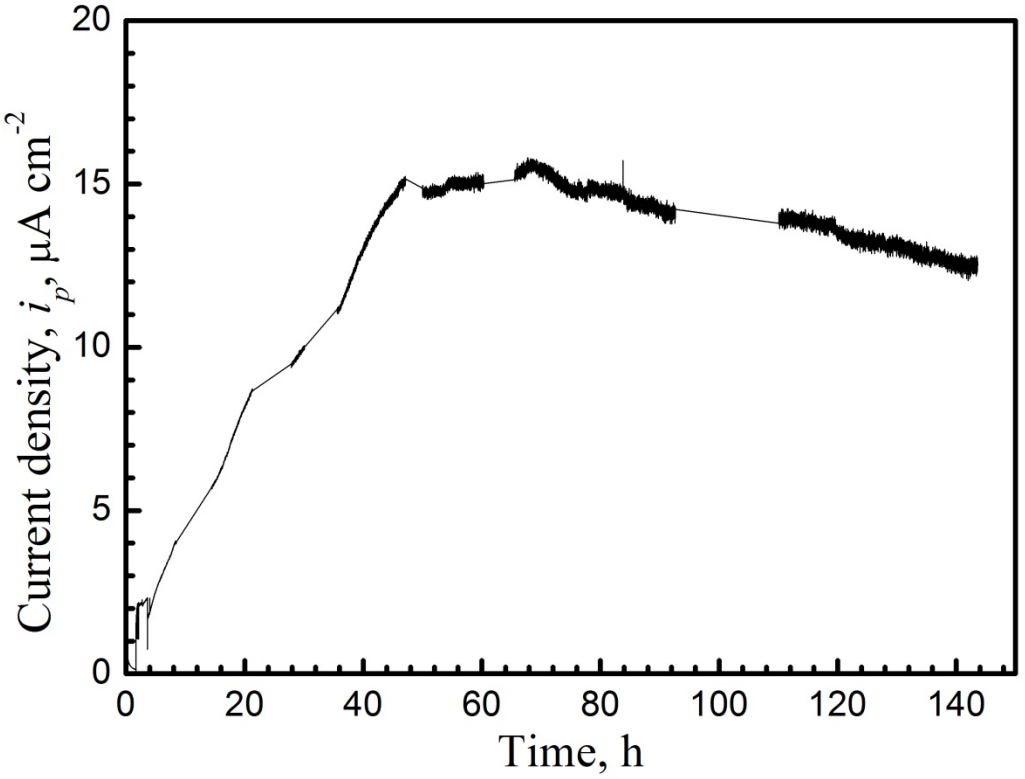

Fig. 6(a) Hydrogen permeation current density, i_p, versus elapsed time during cathodic pre-charging polarisation at -1.500 $V_{Ag/AgCl}$ on the input side of an annealed low interstitial steel membrane in the 0.1 M NaOH solution. Periodically, permeation transients were measured, such as the typical ones presented in Fig. 7. The potential was changed to -1.200 $V_{Ag/AgCl}$, enough time was allowed to elapse until the permeation current density was constant, and a permeation transient was measured between -1.200 $V_{Ag/AgCl}$ to -1.500 $V_{Ag/AgCl}$. The time for the measurement of the permeation transients was subtracted from the elapsed time, and only the time at -1.500 $V_{Ag/AgCl}$ was used.

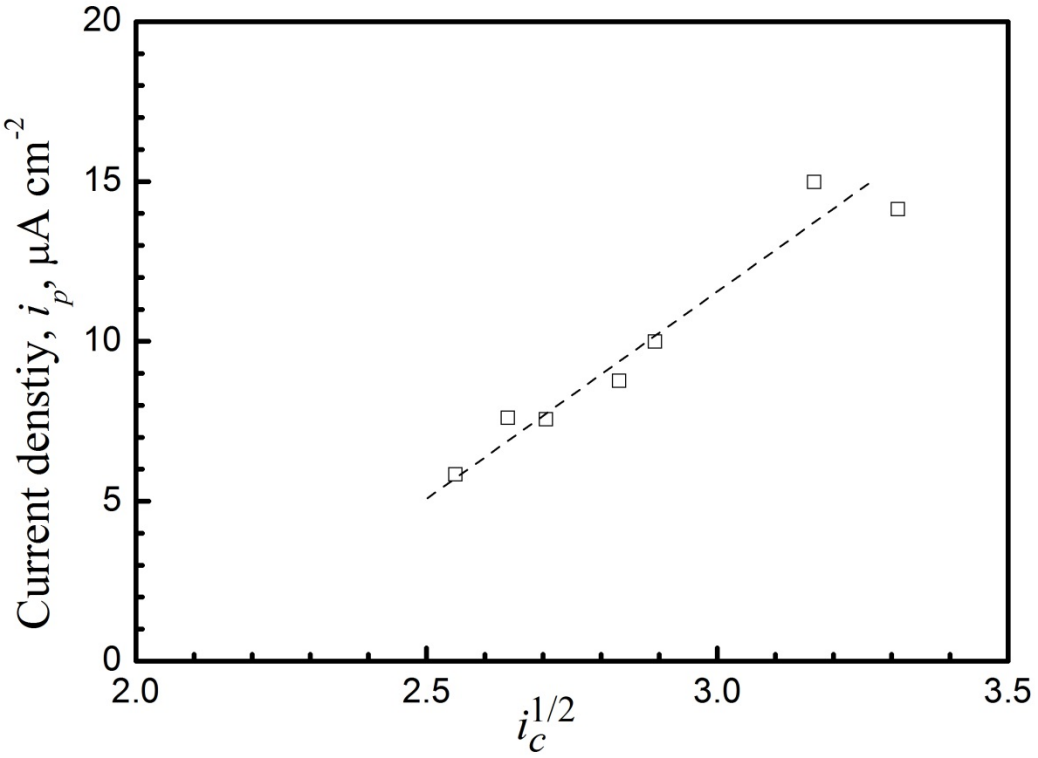

Fig. 6(b) Hydrogen permeation current density versus square root of the charging current density for cathodic pre-charging at a polarisation at -1.500 $V_{Ag/AgCl}$ on the input side of an annealed low interstitial steel membrane (L = 0.88 mm) in the 0.1 M NaOH solution.

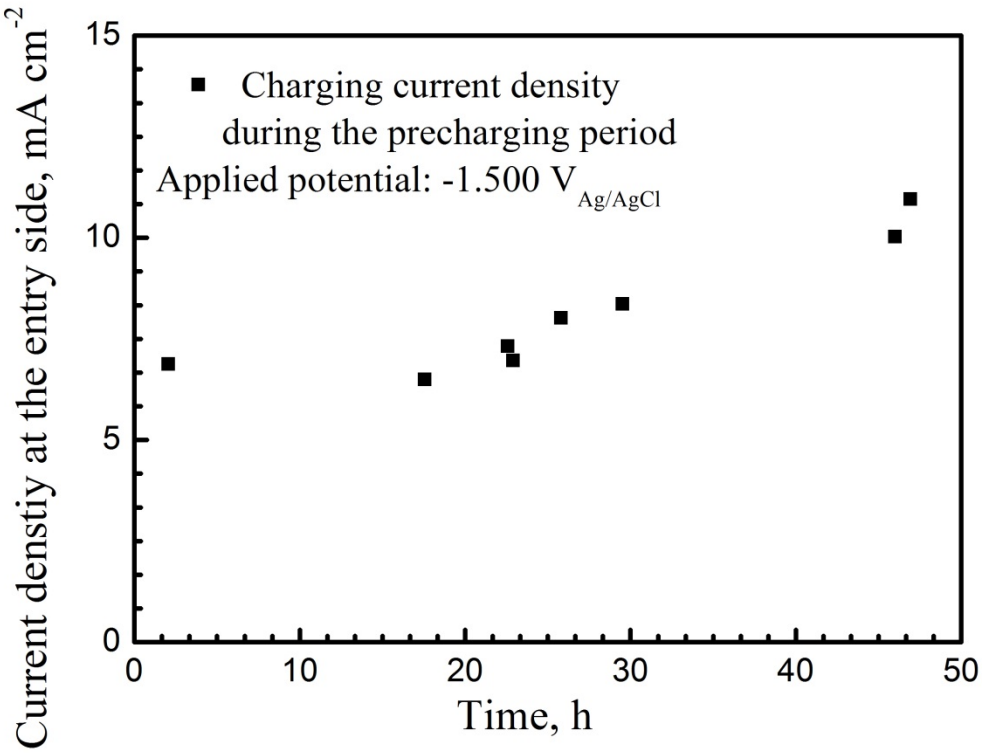

Fig. 6(c) Hydrogen charging current density, i_c, versus charging time for cathodic pre-charging at -1.500 $V_{Ag/AgCl}$ on the input side of an annealed low interstitial steel membrane (L = 0.88 mm) in the 0.1 M NaOH solution.

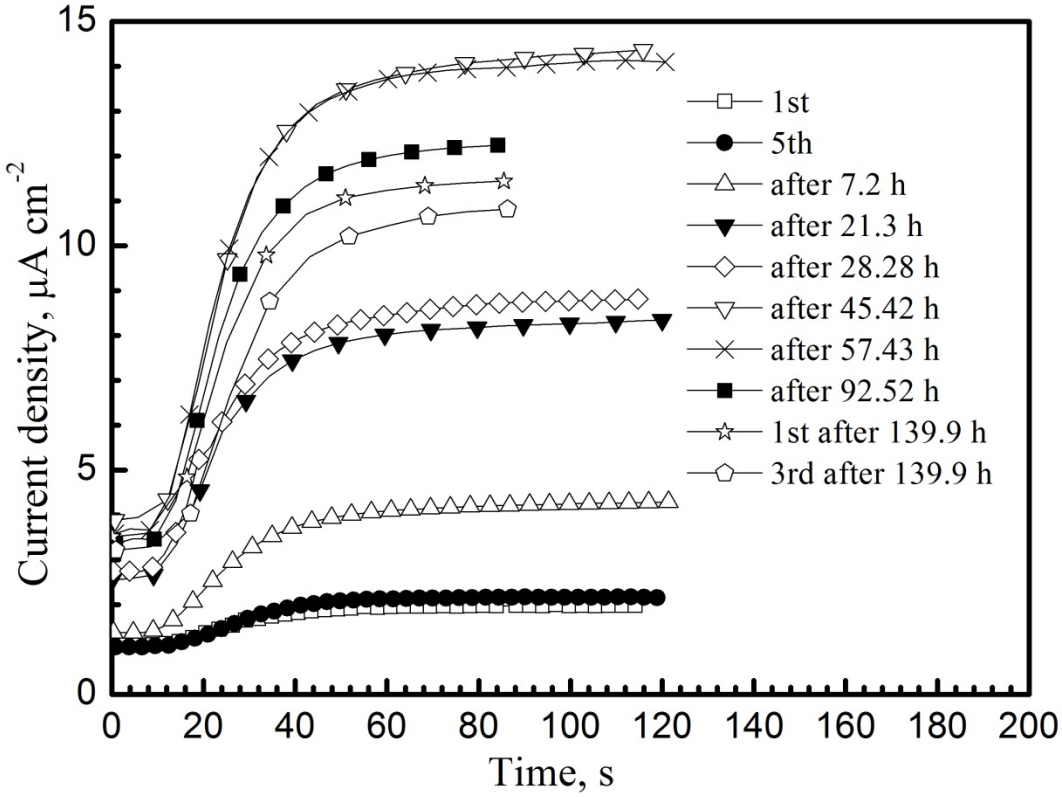

Fig. 7 Hydrogen permeation transients measured after the input potential was changed from -1.200 $V_{Ag/AgCl}$ to -1.500 $V_{Ag/AgCl}$ on the input side of a low interstitial steel membrane in the 0.1 M NaOH solution, and after the stated time with the potential on the input side was maintained stated time at -1.500 $V_{Ag/AgCl}$. After each permeation transient, the potential on the input side was maintained for the stated time at -1.500 $V_{Ag/AgCl}$, until the indicated time to measure the next rise transient, where upon there was a change of input potential and a decay transient (which are not shown), after which was measured the permeation transient shown in the figure.

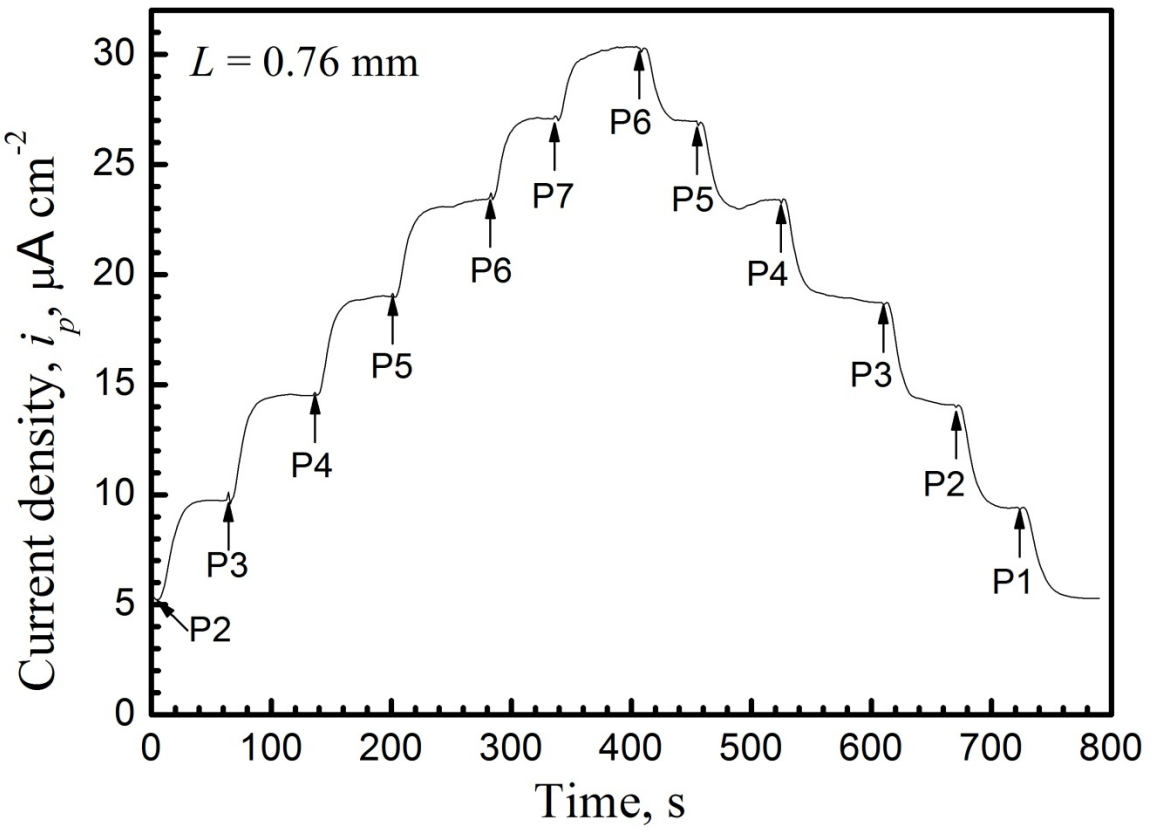

Fig. 8 Hydrogen permeation transients at different cathodic potentials at the input side of the low interstitial steel specimen in the 0.1 M NaOH solution after 48 h charging at -1.500 $V_{Ag/AgCl}$: P1: -1.200 $V_{Ag/AgCl}$; P2: -1.300 $V_{Ag/AgCl}$; P3: -1.400 $V_{Ag/AgCl}$; P4: -1.500 $V_{Ag/AgCl}$; P5: -1.600 $V_{Ag/AgCl}$; P6: -1.700$V_{Ag/AgCl}$; P7: -1.800 $V_{Ag/AgCl}$.

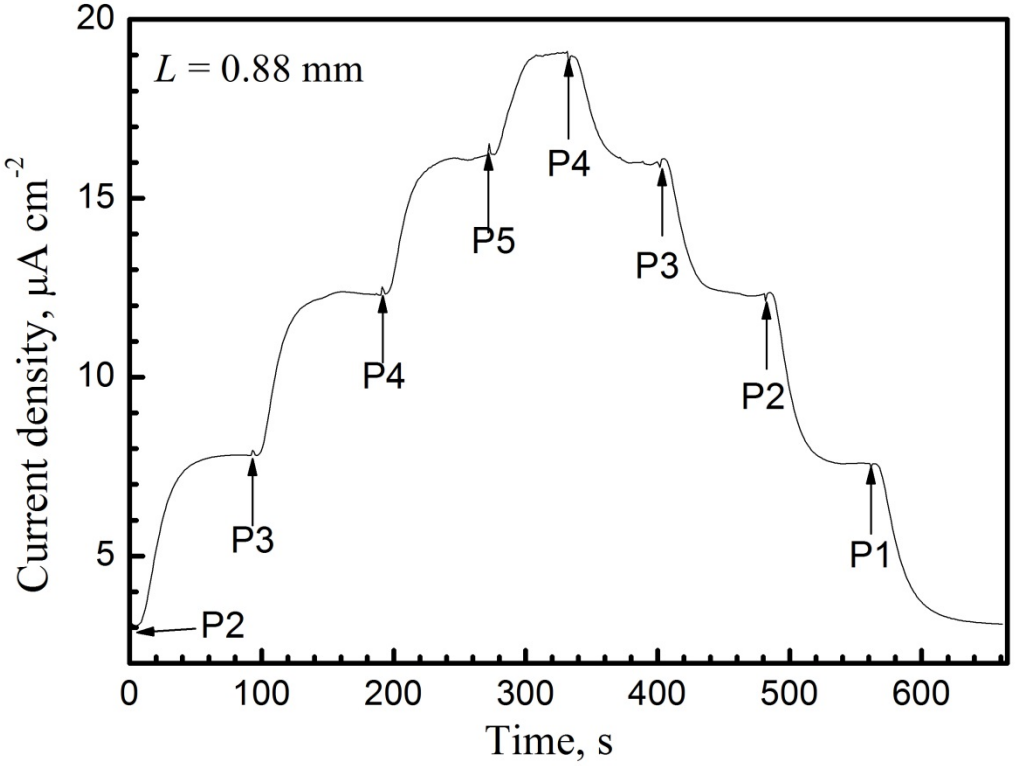

Fig. 9(a) Hydrogen permeation transients at different cathodic potentials at the input side of the low interstitial steel specimen in the 0.1 M NaOH solution after 48 h charging at -1.500 $V_{Ag/AgCl}$: P1: -1.100 $V_{Ag/AgCl}$; P2: -1.250 $V_{Ag/AgCl}$; P3: -1.450 $V_{Ag/AgCl}$; P4: -1.650 $V_{Ag/AgCl}$; P5: -1.850 $V_{Ag/AgCl}$.

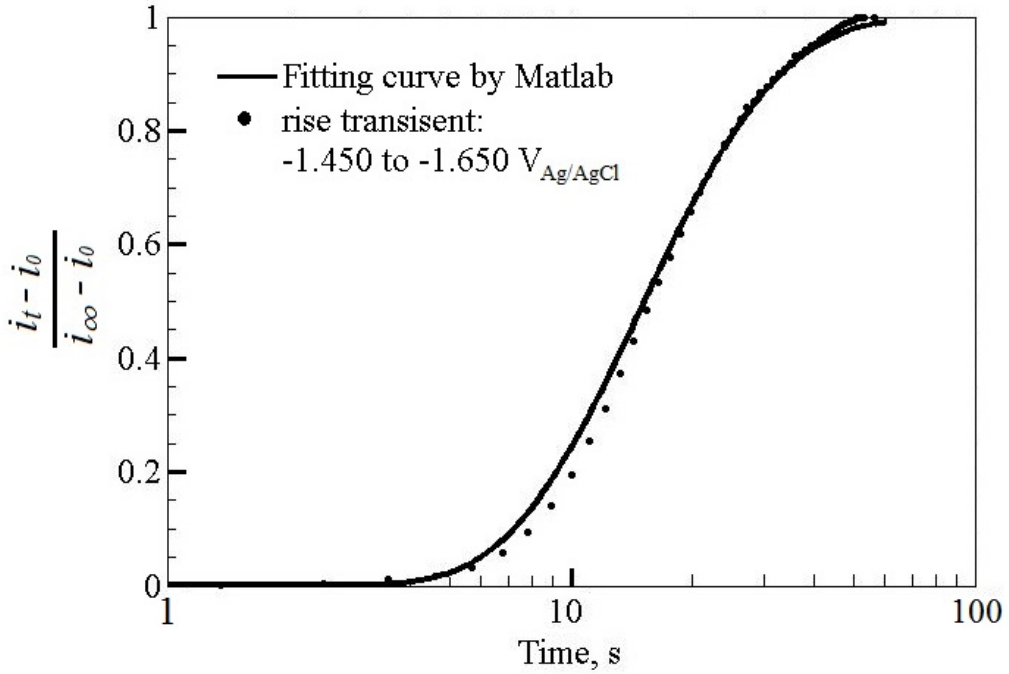

Fig. 9(b) Typical fitting for a permeation rise transient by Matlab for the transient from -1.450 $V_{Ag/AgCl}$ to -1.650 $V_{Ag/AgCl}$ from the sequence of Fig. 9(a) for the low interstitial steel specimen in the 0.1 M NaOH solution after 48 h charging at -1.500 $V_{Ag/AgCl}$.

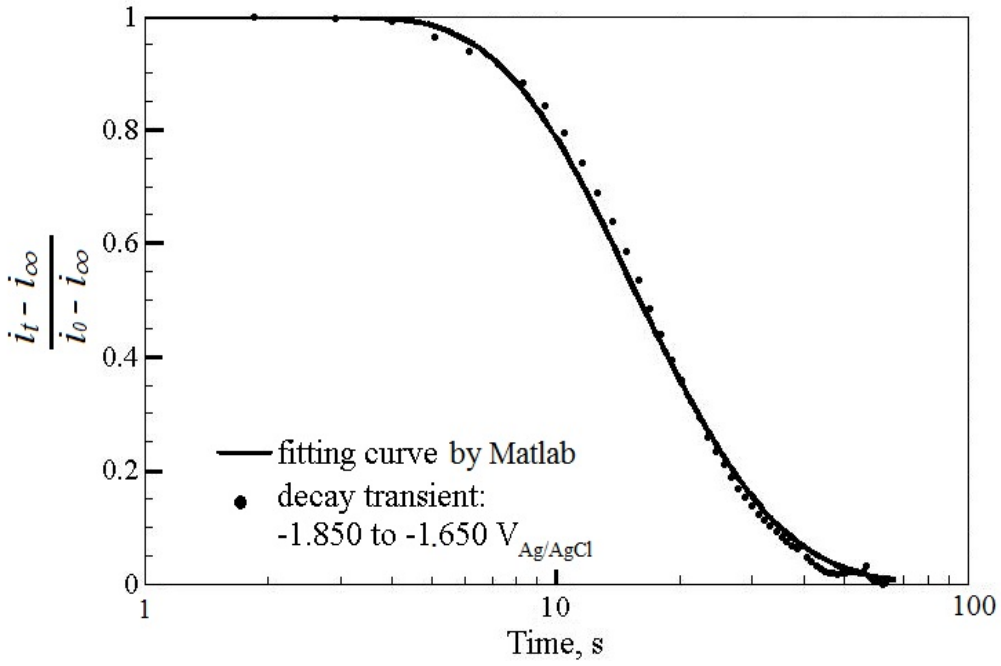

Fig. 9(c) Typical fitting for a permeation decay transient by Matlab for the transient from -1.850 $V_{Ag/AgCl}$ to -1.650 $V_{Ag/AgCl}$ from the sequence of Fig. 9(a) for the low interstitial steel specimen in the 0.1 M NaOH solution after 48 h charging at -1.500 $V_{Ag/AgCl}$.

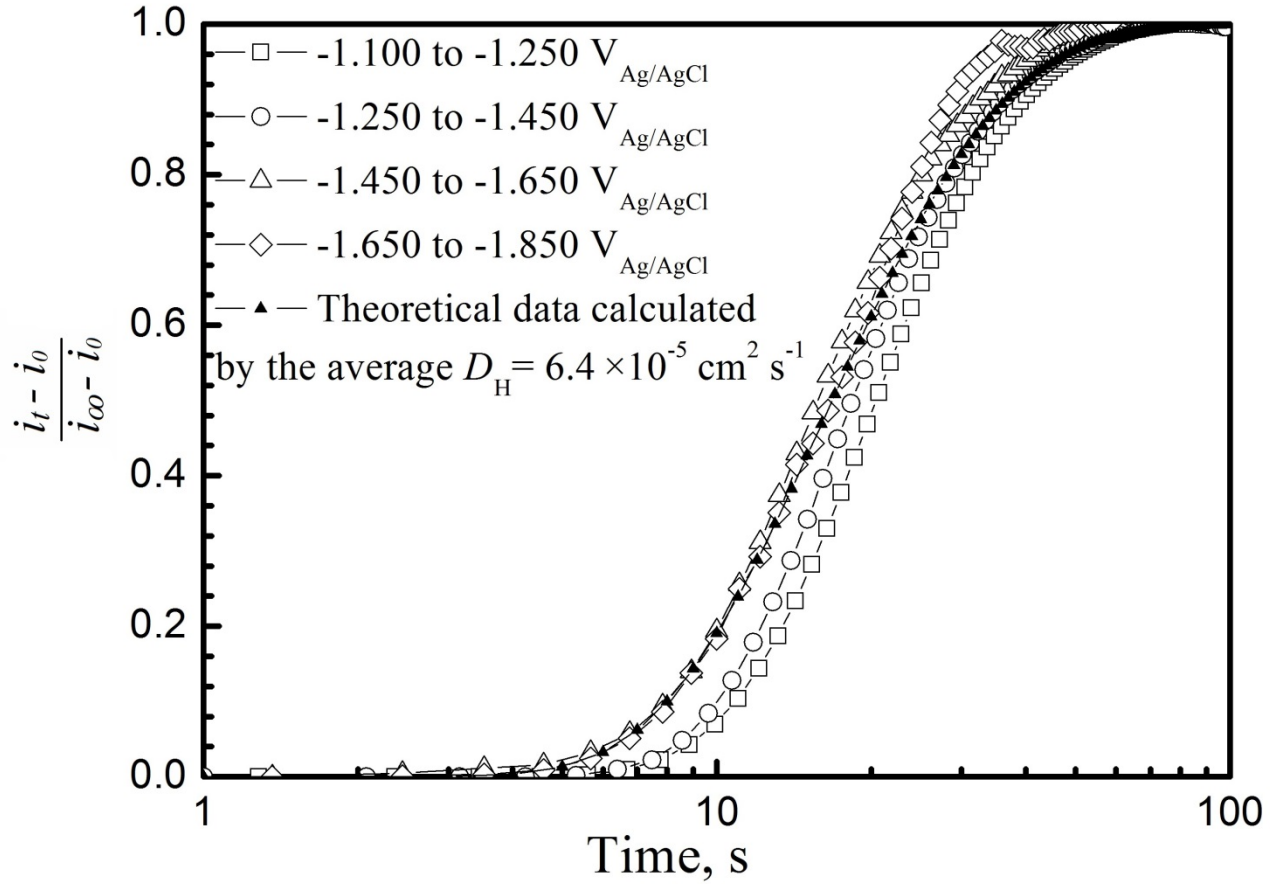

Fig. 9(d) Measured permeation rise transients from the sequence of Fig. 9(a) for the low interstitial steel specimen in the 0.1 M NaOH solution after 48 h charging at -1.500 $V_{Ag/AgCl}$. Also shown is the theoretical rise transient calculated with the average value of the diffusion coefficient.

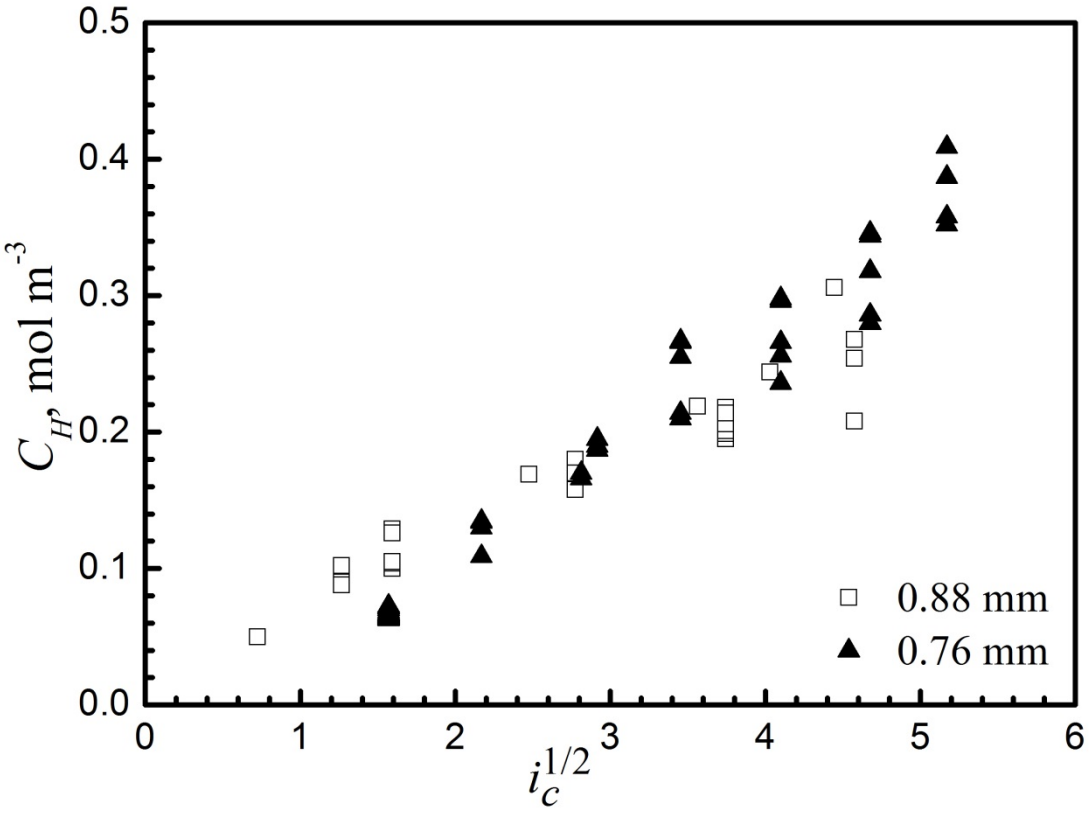

Fig. 10 The hydrogen concentration, C_H (mol m^{-3}), at the entry side of a low interstitial steel specimen vs. the square root of cathodic charging current density, i_c (mA cm^{-2}). The data were obtained using the 0.1 M NaOH solution on the input side of the permeation cell.

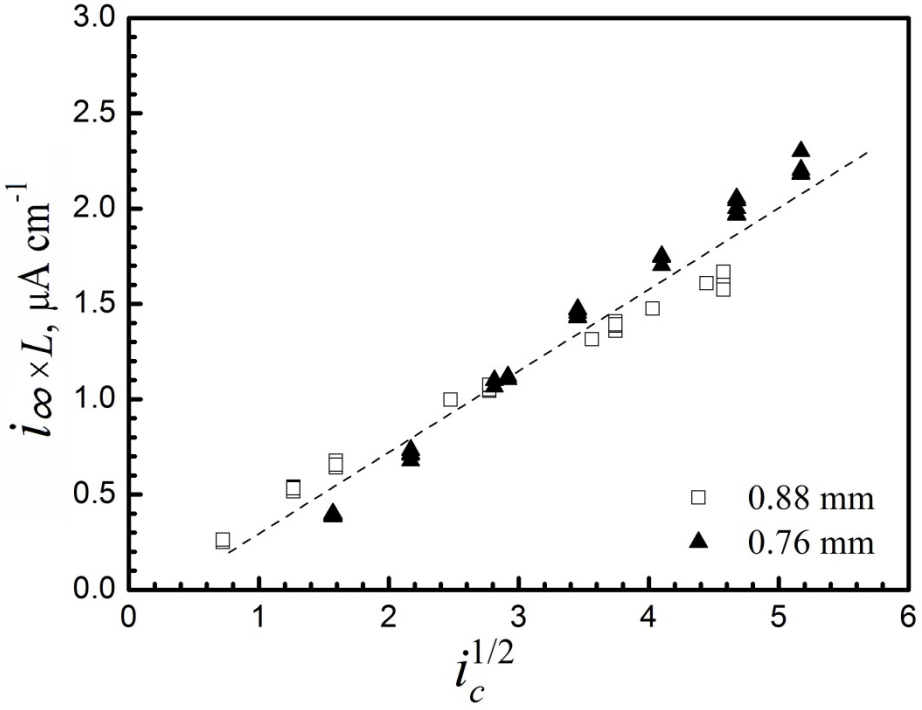

Fig. 11 The steady-state hydrogen permeation rate, i_∞ (μA cm^{-2}), multiplied by the specimen thickness, L, for a low interstitial steel specimen vs. the square root of cathodic charging current density, i_c (mA cm^{-2}). The data were obtained using the 0.1 M NaOH solution in the input side of the permeation cell.

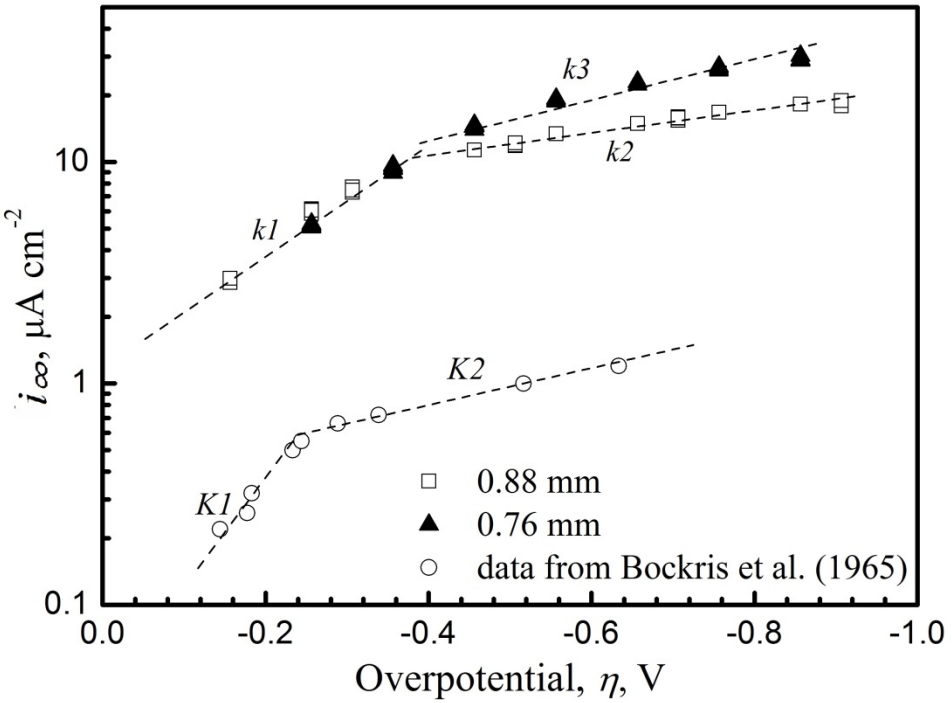

Fig. 12 The steady-state hydrogen permeation rate, i_∞ (μA cm^{-2}), vs. the overpotential, η (V), for the low interstitial steel (triangles and squares). The data were obtained using the 0.1 M NaOH solution in the input side of the permeation cell. The circles represent data from Bockris et al. [79] in the same solution.

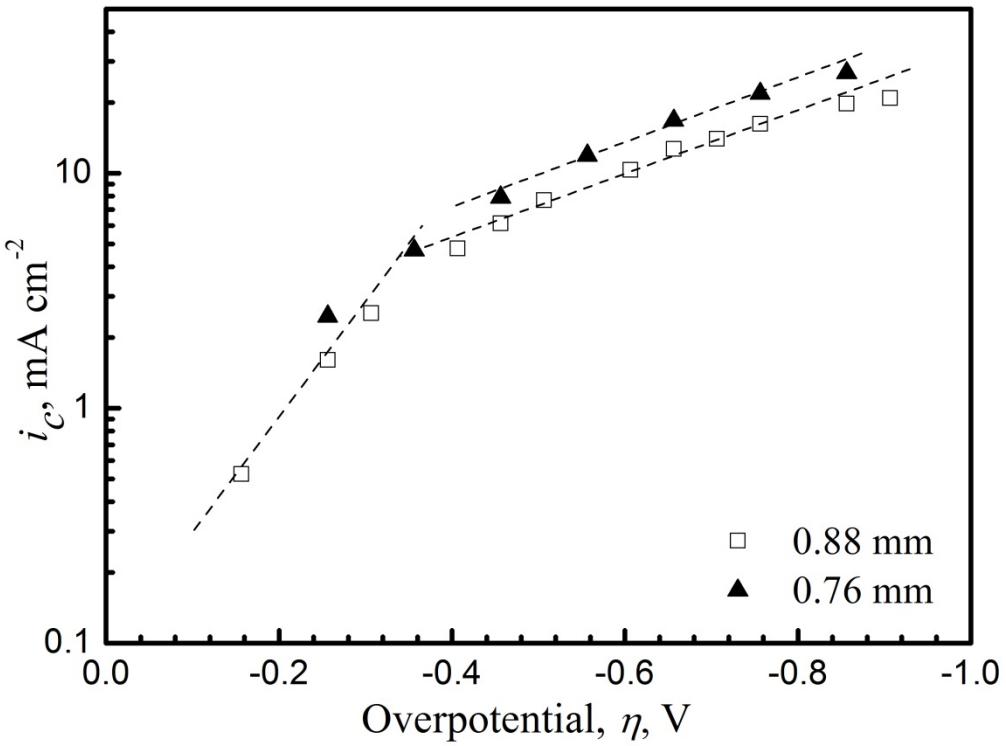

Fig. 13 The charging current density, i_c (mA cm^{-2}), on the input side of the low interstitial steel specimen vs. overpotential, η (V). The data were obtained using the 0.1 M NaOH solution in the input side of the permeation cell.

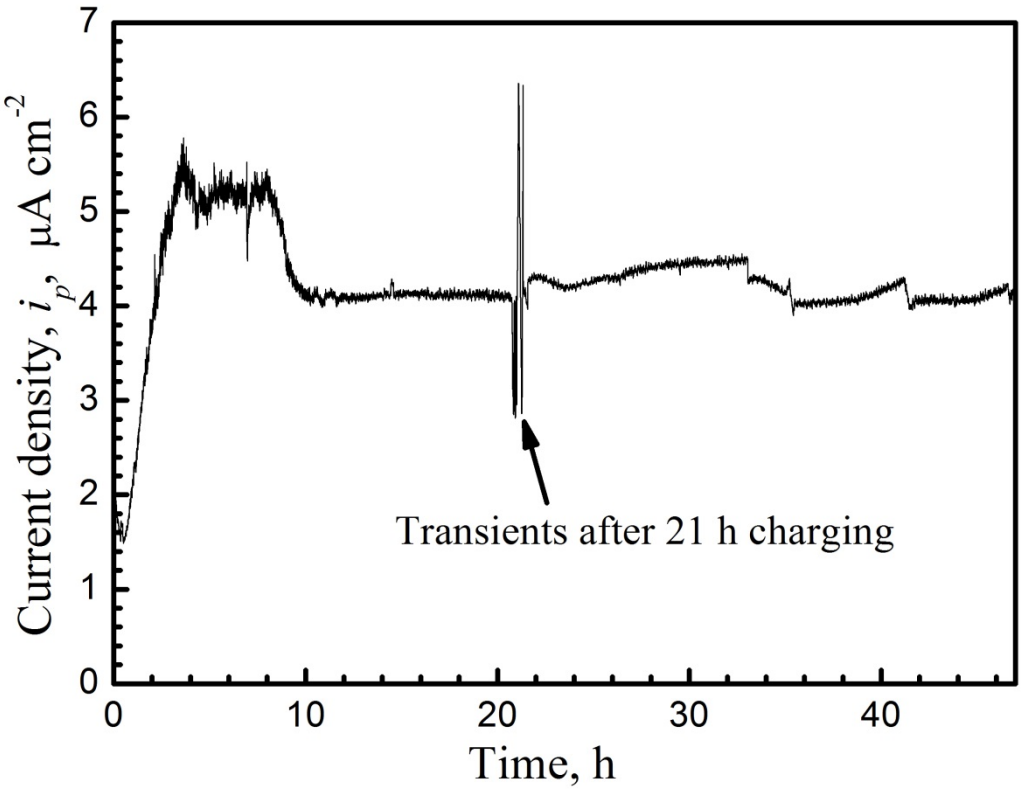

Fig. 14 Hydrogen permeation current density versus time of cathodic polarisation at -1.400 $V_{Ag/AgCl}$ of the low interstitial steel specimen in the acidified pH 2 0.1 M Na_2SO_4 solution. The magnified view of the transients after 21 h charging are presented in Fig. 15.

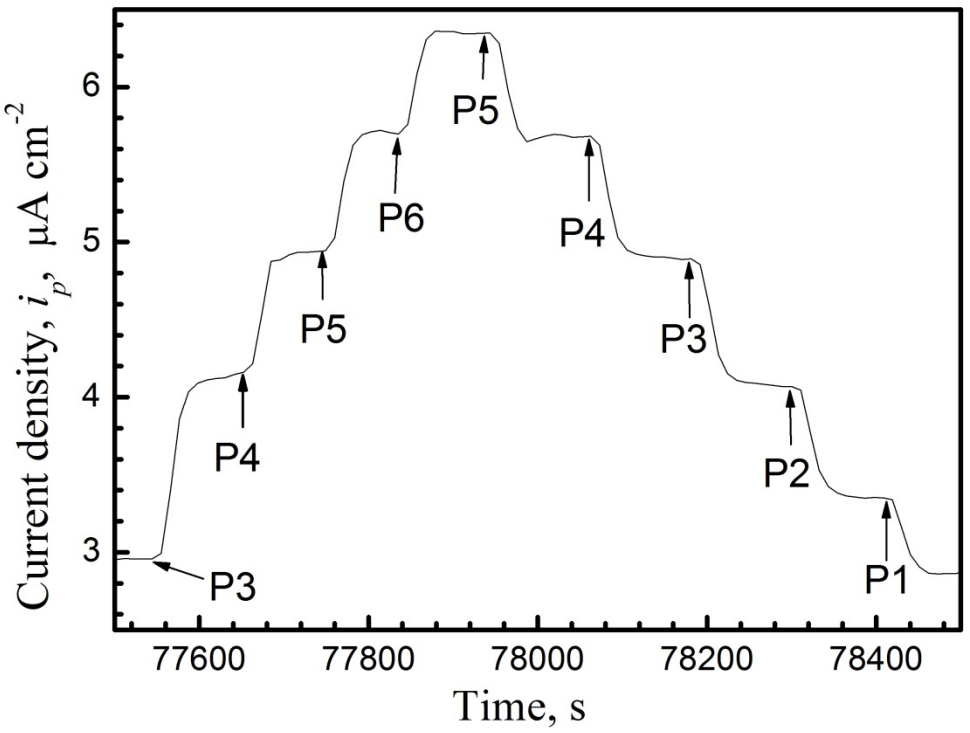

Fig. 15 Hydrogen permeation transients for a low interstitial steel at different cathodic potentials in the pH 2 0.1 M Na_2SO_4 solution on the charging side after charging at -1.400 $V_{Ag/AgCl}$ for 21 h: P1: -1.200 $V_{Ag/AgCl}$; P2: -1.300 $V_{Ag/AgCl}$; P3: -1.400 $V_{Ag/AgCl}$; P4: -1.500 $V_{Ag/AgCl}$; P5: -1.600 $V_{Ag/AgCl}$; and P6: -1.700 $V_{Ag/AgCl}$.

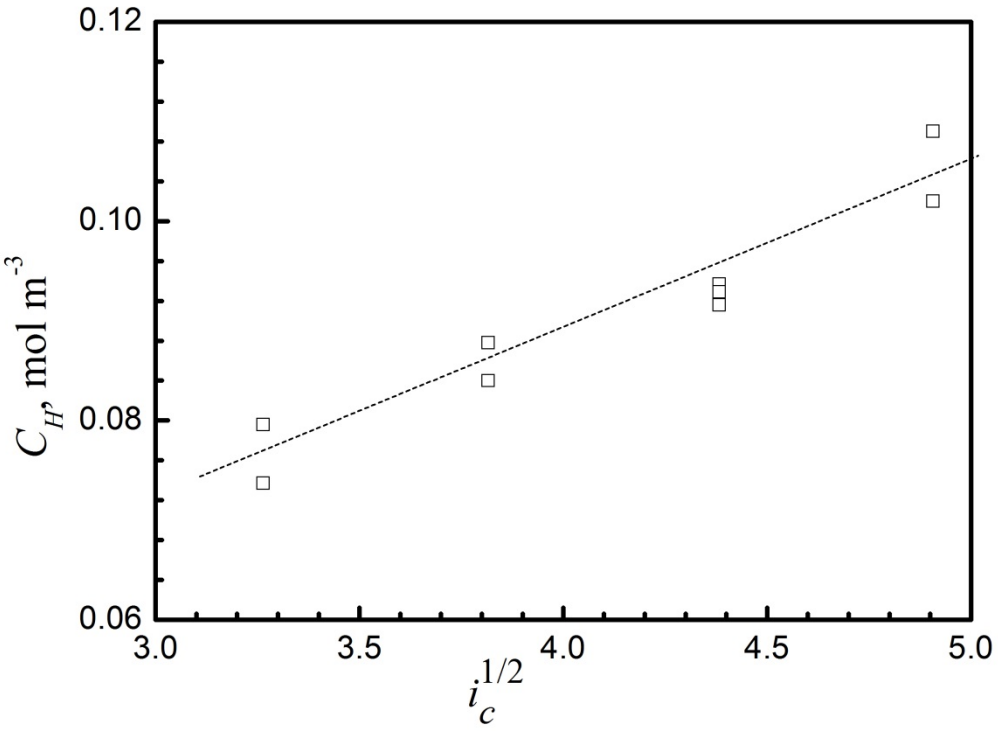

Fig. 16 The hydrogen concentration, C_H (mol m^{-3}), at the entry side for a low interstitial steel specimen vs. the square root of cathodic charging current density, i_c (mA cm^{-2}) at the entry side. The data were obtained in the pH 2 0.1 M Na_2SO_4 solution.

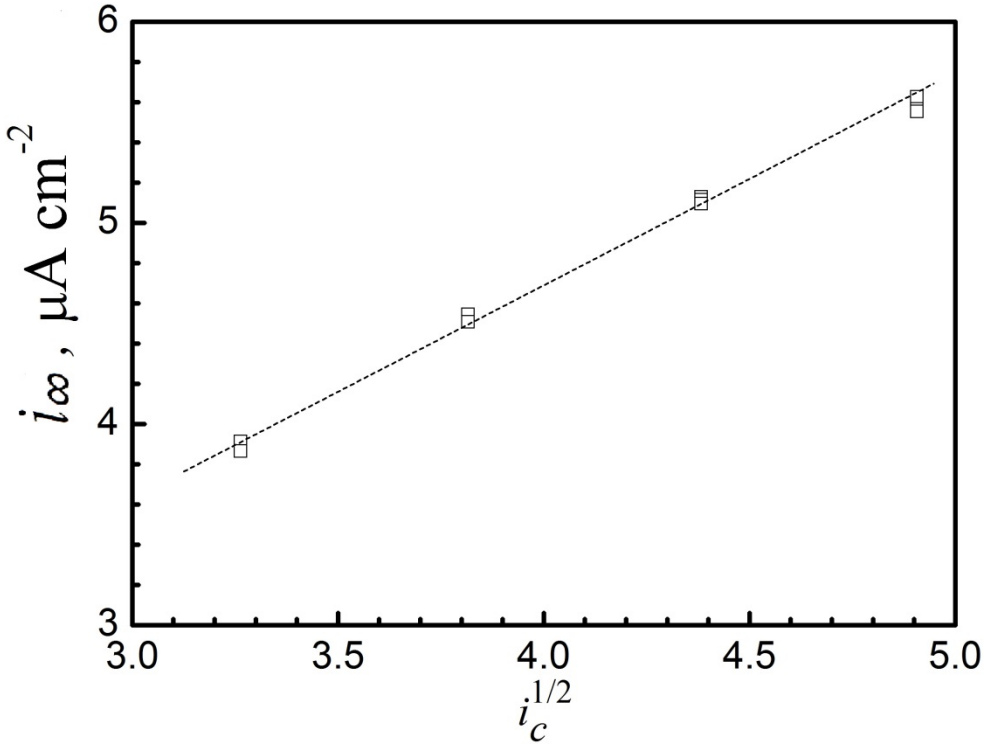

Fig. 17 The steady-state hydrogen permeation rate, i_∞ (μA cm^{-2}), for a low interstitial steel specimen vs. the square root of cathodic charging current density, i_c (mA cm^{-2}). The data were obtained using the pH 2 0.1 M Na_2SO_4 solution in the input side of the permeation cell.

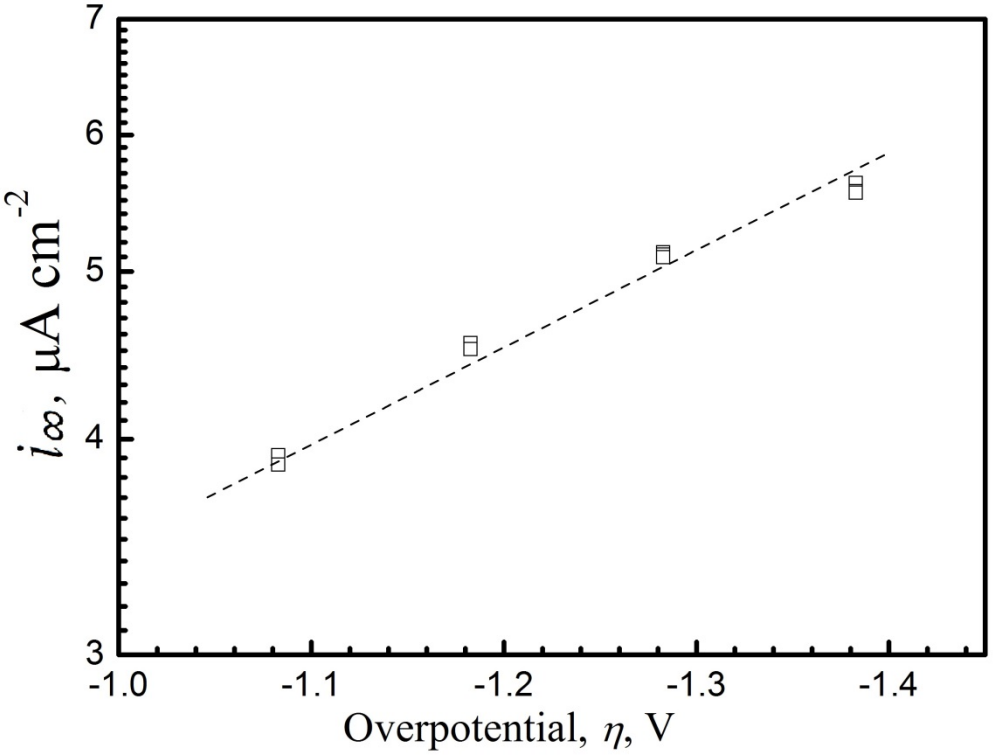

Fig. 18 The steady-state hydrogen permeation rate, i_∞ (μA cm^{-2}), for a low interstitial steel specimen vs. the overpotential, η (V). The data were obtained using the pH 2 0.1 M Na_2SO_4 solution in the input side of the permeation cell.

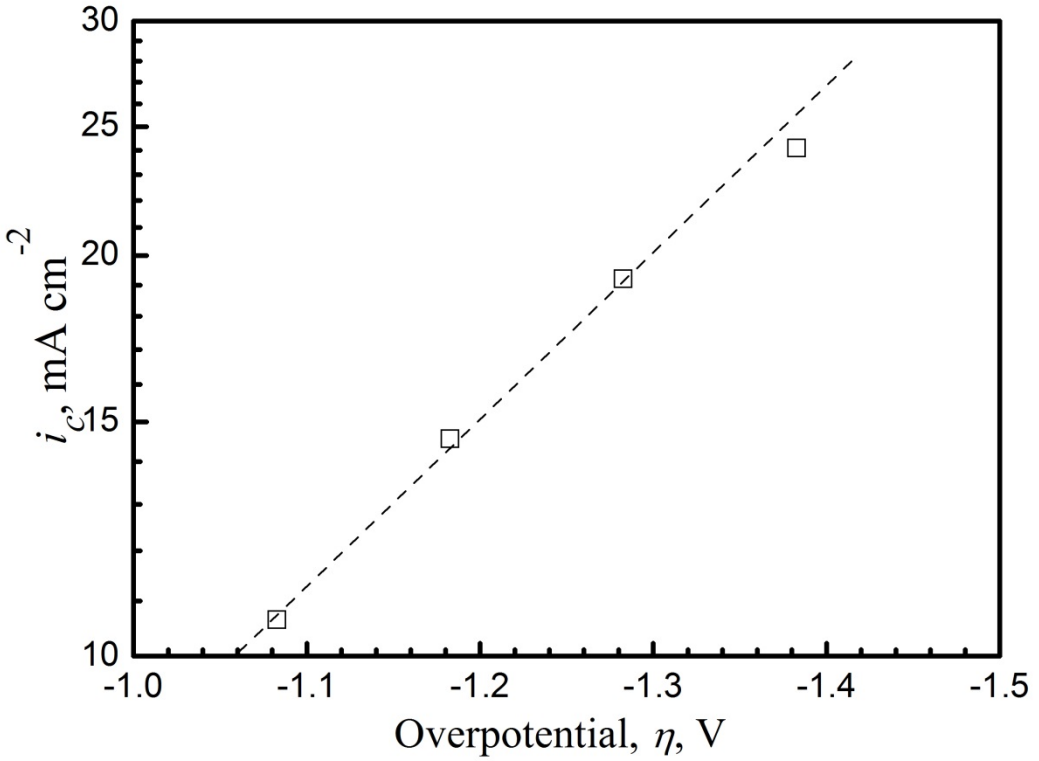

Fig. 19 The charging current density, i_c (mA cm^{-2}), on the input side for a low interstitial steel specimen vs. overpotential, η (V). The data were obtained using the pH 2 0.1 M Na_2SO_4 solution in the input side of the permeation cell.

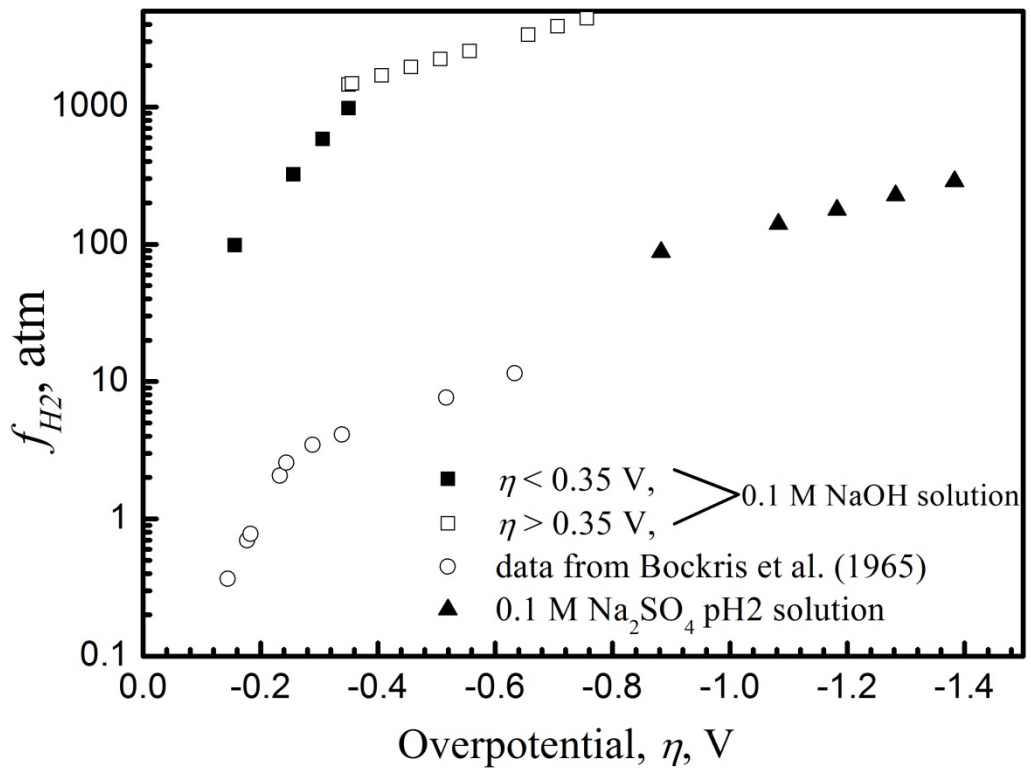

Fig. 20 The relationship between hydrogen fugacity, f_{H2}, and overpotential, η (V), evaluated from permeability transients for the low interstitial steel in (i) 0.1 M NaOH solution, and (ii) acidified pH 2 0.1 M Na_2SO_4 solution in the input side of the permeation cell. The valued pertaining to the open circles were calculated from the Bockris et al. [79] permeation data in the 0.1 M NaOH solution.

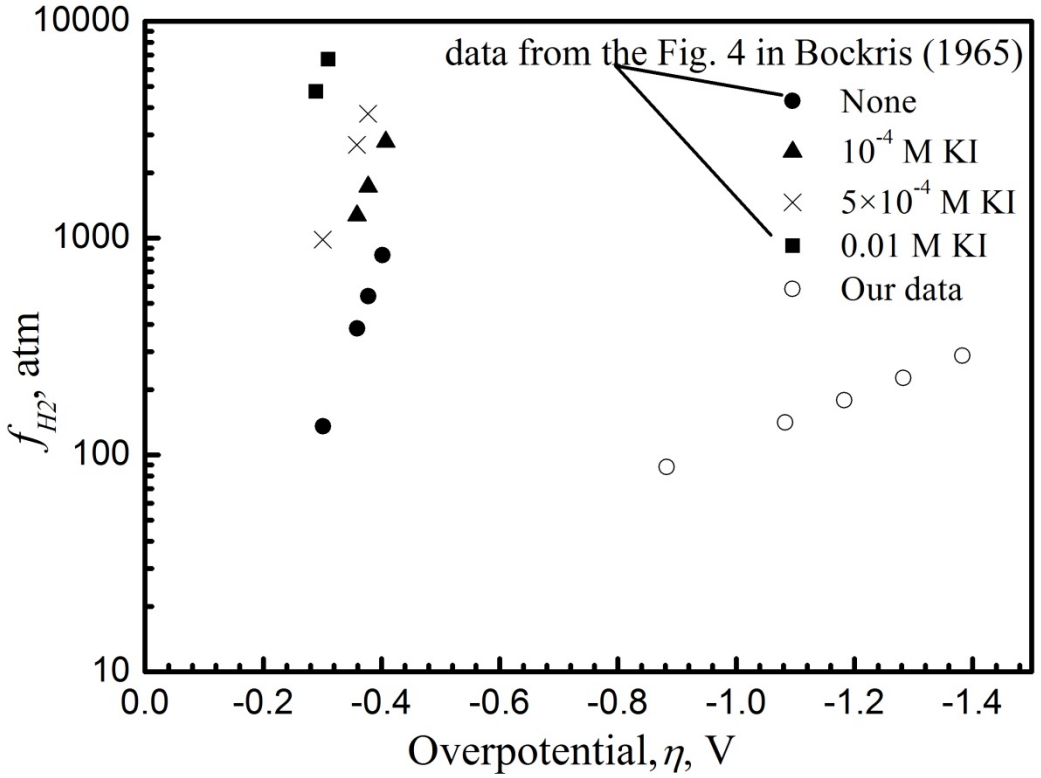

Fig. 21 Relationship between hydrogen fugacity (evaluated applying the above methodology to the data of Bockris et al. [79]) for pure iron for low values of overpotential in 0.1 N H_2SO_4 with various additions of KI, compared with our evaluation of the relationship between hydrogen fugacity, f_{H2}, and overpotential, η (V), evaluated from permeability transients for low interstitial steel specimens in the acidified pH 2 0.1 M Na_2SO_4 solution in the input side of the permeation cell.

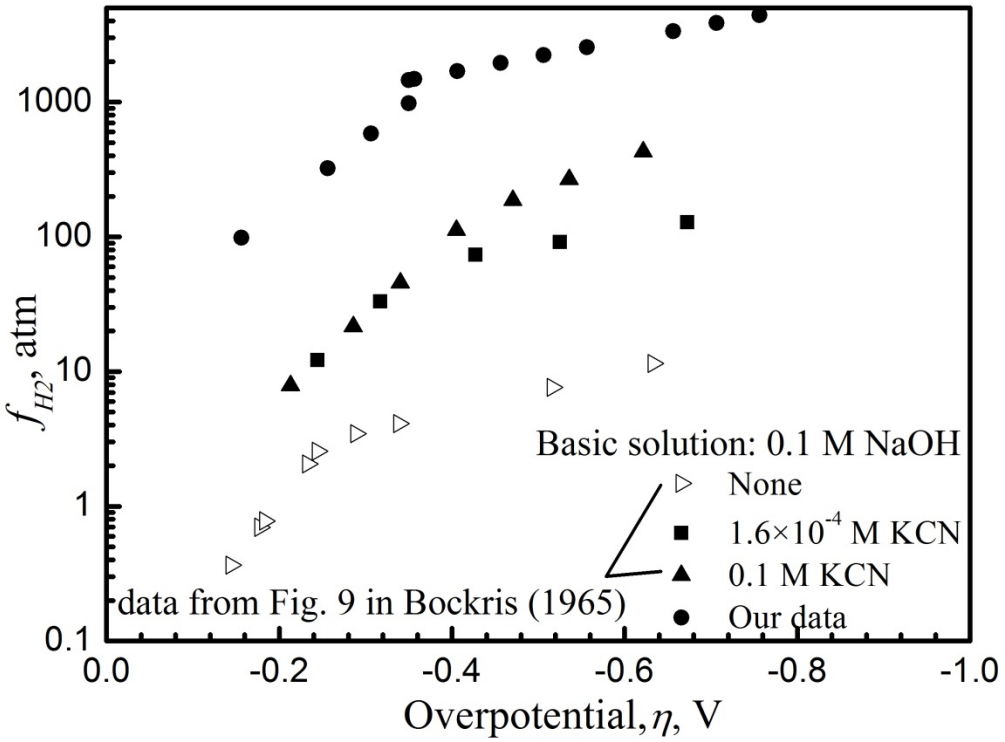

Fig. 22 Relationship between hydrogen fugacity (evaluated applying the above methodology to the data of Bockris et al. [79]) for pure iron in 0.1 M NaOH solution with various additions of KCN, compared with our evaluation of the relationship between hydrogen fugacity, f_{H2}, and overpotential, η (V), evaluated from permeability transients for low interstitial steel specimens in the 0.1 M NaOH solution in the input side of the permeation cell.